Mechanisms for light charged particle emission in the reactions 247 and 337 MeV $^{40}Ar + ^{nat}Ag$

Roy Lacey, N. N. Ajitanand,* John M. Alexander, D. M. de Castro Rizzo, G. F. Peaslee, and L. C. Vaz
Department of Chemistry, State University of New York at Stony Brook, Stony Brook, New York 11794

Morton Kaplan, M. Kildir,† G. La Rana,‡ D. J. Moses, and W. E. Parker
Department of Chemistry, Carnegie-Mellon University, Pittsburgh, Pennsylvania 15213

D. Logan§ and M. S. Zisman
Lawrence Berkeley Laboratory, Berkeley, California 94720

P. DeYoung**
Department of Physics, State University of New York at Stony Brook, Stony Brook, New York 11794

L. Kowalski
Department of Physics & Geoscience, Montclair State College, Upper Montclair, New Jersey 07043
(Received 28 December 1987)

Light charged particles from the reactions 247 and 337 MeV $^{40}Ar + ^{nat}Ag$ have been measured in singles and in coincidence with fission-like products. Most of the ^{1}H and ^{4}He in coincidence with fusion-fission and quasifission can be accounted for by evaporation from the composite nucleus or by the fragments. Multiplicities are determined for ^{1}H and ^{4}He in association with evaporation residues, fusion-fission, and quasifission. The probability for composite nucleus emission decreases with increasing spin zone of the emitter and gives a view of the role of emitter lifetime. The ratio of composite-nucleus multiplicities for quasifission/fusion-fission is about $\frac{1}{2}$ ($\frac{1}{4}$) for 337 MeV ^{40}Ar (247 MeV ^{40}Ar) which implies a similar ratio for the lifetimes of the respective composite nuclei between thermalization and scission. Energy spectra and angular distributions of particles (in coincidence with fusion-fission and quasifission) are consistent with emission from a strongly distorted nuclear system en route toward scission. Prethermalization emission of ^{4}He is observed at 10° in comparable amounts for peripheral collisions (quasifission and fusion-fission) and for central collisions.

I. INTRODUCTION

When nuclei are excited to temperatures of about 1 MeV or more, their deexcitation gives rise to many light particles with continuous Maxwellian-like spectra. There have been a number of measurements of the energy and angular distributions of these continuum particles. A satisfying interpretation of these observations requires first a qualitative characterization of the production mechanism(s) and second a model that allows a quantitative link to the properties of the emitter (or daughter) nuclei. In heavy-ion reactions with $E/A \leq 20$ MeV, fusion and deeply inelastic (or quasifission) reactions constitute the major mechanisms for producing highly excited nuclei.[1] Their subsequent evaporation chains constitute the main sources of continuum particle spectra at backward angles (with respect to the light collision partner). See, for example, Refs. 2 and 3 and other references therein.

In recent years there has been strong interest in the determination of the active emitter nuclei and in attempts to infer their statistical properties (see, for example, Refs. 4–20.) Coincidence measurements have allowed a separation of the particles according to the velocity of the emitter and then a subsequent characterization of the intrinsic energy and angular distributions. In particular a number of experiments have reported multiplicities for particle emission from the composite nucleus and/or from fully accelerated products of fusion fission (FF) or quasifission (QF) (see, for example, Refs. 3, 5, 10, 14, 15, 19, and 21–32.)

An interesting result has been the large amount of composite-nucleus evaporation (CE) in competition with fission, even for very hot and very fissile nuclei. Evaporation spectra have been reported for composite nuclei with temperatures of up to ≈ 5 MeV.[15] Statistical model calculations[33,34] have been used to interpret these spectra in terms of emitter (or daughter) properties such as root-mean-square spin, temperature, moment of inertia, and effective deformation (see, for example, Refs. 35–37).

In this work we have chosen two reaction systems of intermediate fissility, 247 and 337 MeV $^{40}Ar + ^{nat}Ag \rightarrow ^{147,9}Tb^*$. For these reactions the cross sections for fissionlike reactions and evaporation residue production (ER) are comparable. For 337 MeV $^{40}Ar + Ag$ the heavy-fragment cross sections[38] indicate spin zones of about $0-70\hbar$ for ER production, $\approx 70-103\hbar$ for FF and $\approx 103-133\hbar$ for QF. For 247 MeV $^{40}Ar + Ag$ the corresponding spin zones are $\approx 0-68\hbar$ for the ER's, $\approx 68-94\hbar$ for FF and $\approx 94-108\hbar$

for QF. Thus we use particle-fragment coincidences to study ^{1}H and ^{4}He emission from two very high-spin zones, and by varying the beam energy we study the temperature dependence for each spin zone. In addition, we have found very large charged-particle multiplicities for the ER's (2–5 ^{1}H and ^{4}He per reaction). This result stimulated us to make a detailed study of the evaporation chains that give ER's by use of particle-particle coincidences. A sketch of some of these ER studies has been published;[36] and a more complete presentation will follow.[39]

Our objective in this paper is to separate the particles associated with FF and QF reactions according to mechanistic origin. To this end, we present inclusive data in Sec. III, and fragment-particle coincidence data in Sec. IV. We interpret these results via the reaction simulation code GANES (Ref. 37) that uses statistical-model theory along with detailed considerations of the reaction kinematics.[37] In Sec. V we examine the mechanistic implications of the fragment-particle coincidence data. We have determined angle-integrated multiplicities for composite-nucleus and fragment evaporation processes in both FF and QF. Most particles are assigned to evaporation from composite nuclei and fully accelerated fragments. Nevertheless some indications are found for near-scission emission and shadowing. The CE multiplicities decrease with increasing spin of the reaction zone, but there is still enough ^{1}H and ^{4}He emission in both FF and QF to give insights into the properties of the composite nuclei prior to scission. The ratio of CE multiplicities for QF/FF is about $\frac{1}{2}$ for 337 MeV ^{40}Ar, which implies a similar ratio between the times necessary for thermalization and scission. The energy and angular distributions indicate that evaporation often occurs as the composite system is strongly distorted and enroute towards binary breakup.

II. EXPERIMENTAL SETUP, TECHNIQUES, AND UNCERTAINTIES

A. Experimental overview

The super heavy ion linear accelerator (superHILAC) at the Lawrence Berkeley Laboratory provided the argon beams used in these experiments. Beams of 247 and 337 MeV from the accelerator were defined by four-jaw and circular collimators[40] before impinging on the ^{nat}Ag target inside a 60 in scattering chamber. The collimation system provided a well-defined beam spot ($\approx$3 mm diameter) at the target center and the beam was monitored downstream from the target by a faraday cup. The ^{nat}Ag targets used were self-supporting and their thicknesses (600–900 μg/cm^2) were measured relative to an Au target of known thickness by elastic scattering. Average beam currents were $\approx$60 nA and $\approx$2 nA (electrical) for coincidence and inclusive measurements, respectively.

Fusion fission and quasifission fragments[38] were detected in gas ionization telescopes (GT) (40 Torr hexane and 300 μm Si stopping detector) subtending $\approx$4 msr.[41] The ΔE and E signals from the GT provided Z identification of the heavy fragments with a resolution of $\approx$3 units. Light charged particles (^{1,2,3}H,^{4}He) were detected in solid-state telescopes (SST) (50 μm, 500 μm, 5 mm) and two wedge detectors, each with ionization chambers for ΔE signals and five Si stopping detectors.[40] Solid angles subtended by the light charged particle detectors were $\approx$5 msr. Typical thresholds for the SST's were $\approx$2 MeV and $\approx$10 MeV for ^{1}H and ^{4}He, respectively (cover foils were 10 mg/cm^2 of Pb). Thresholds for the wedge detectors were generally lower, $\approx$3 MeV for ^{4}He (cover foils of 3 mg/cm^2 Au); these wedge detectors did not separate the H isotopes.

Energy calibrations for each Si detector were accomplished by reference to a ^{212}Pb alpha source. A ^{252}Cf fission source and the elastically scattered beam were employed for GT calibrations.[42] Solid angles were determined from measured rates of α-particle detection from calibrated radioactive sources mounted at the target position, as well as from geometric measurements.[40]

B. Experimental geometry

Figure 1 shows the experimental setup used for one of three experiments performed. Alpha particles were detected in two wedge detectors (mounted in the horizontal plane) centered at $\theta=-85°$, and $\theta=135°$ (θ is measured with respect to the beam). These two banks of ^{4}He detectors were triggered by heavy fragments (FF and QF)

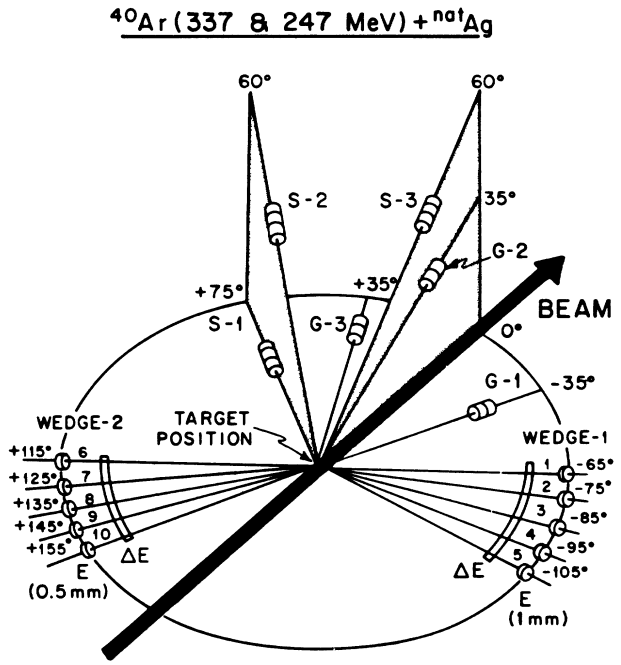

FIG. 1. Detector setup for this study of the reactions 247 and 337 MeV ^{40}Ar + ^{nat}Ag. Heavy fragments are detected in three gas ionization telescopes (G-1,-2,3). Light charged particles (H and He) were detected in three solid state telescopes (S-1,-2,-3) and two $\Delta E-E$ wedge detectors (W-1 and W-2).

in gas telescopes G-1, -2, or -3 each mounted at $\theta=35°$ or by ^{1,2,3}H or ^{4}He in solid-state telescopes S-1 ($\theta=75°$), S-2 ($\theta=83°$), or S-3 ($\theta=60°$). Out-of-plane angles are given in Fig. 1. Data were recorded in the coincidence modes described above and also in the singles mode for each detector. Setups for the other experiments all had the same angle between GT and the beam, but the particle detectors were arranged differently.

The experimental setups were guided by a desire to make extensive angular distribution measurements for the particles with a geometry which was also effective for disentangling fragment and composite emission (FE and CE). Optimization of the geometry to fully exploit the kinematic shifts associated with FE and CE was guided by the velocity diagrams shown and discussed below. For evaporative emission a substantial angular range ($65° \leq \theta \leq 155°$) was covered in 10° increments by the wedge detectors. Angular distributions of the ^{4}He particles were measured in the wedge detectors in coincidence with light-charged particles or heavy fragments detected in two mutually perpendicular planes. One plane, defined by the beam and S-1, G-1, or G-3, was congruent with the plane in which the wedge detectors were situated (the horizontal plane). The other plane (orthogonal to the first) was defined by the beam and trigger detectors G-2 or S-3. It is important to recognize that these two experimentally defined reaction planes allowed the simultaneous measurement of in-plane and out-of-plane angular distributions for all triggers. In addition, the particle triggers (H/He) selected events from the lowest l window of the entrance channel spin distribution[3,36,43,44] while the fragment triggers selected events associated with the higher l windows for fission and quasifission.[38]

C. Averaging procedure and uncertainties

The experimental results presented in the following sections were taken from three separate experiments performed in subsequent years. Consequently, many of the results were averaged over many experimental runs from these separate experiments. Two methods of averaging were employed. The first was the averaging of results obtained in many runs from a single experiment. This was carried out by simply merging the data from individual runs. From the second method, an arithmetic mean was evaluated for the results from different experiments.

Three general types of measurements were performed: (a) inclusive measurements of light-charged particles and fragments, (b) fragment-particle correlations, and (c) particle-particle correlations. In this paper we consider only the first two types; the third is treated elsewhere.[36,39] For all of the experiments performed, a more comprehensive data set was obtained for ^{4}He, than for ^{1,2,3}H. This is because the wedge detectors which provided low detection thresholds for α particles (particularly important for detection in the backward hemisphere), did not allow separation between the ^{1,2,3}H isotopes. Most of the data for ^{1,2,3}H were provided by SST's which allowed good identification for ^{1,2,3}H and ^{4}He in all of the experiments. The combined results (from all experiments) of these strategically placed detector telescopes were nevertheless sufficient to draw unambiguous conclusions, even for the ^{1,2,3}H isotopes.

Statistical errors associated with results obtained from measurements performed with 337 MeV ^{40}Ar are generally much smaller than those from similar measurements performed at 247 MeV. This is a natural consequence of the smaller number of runs performed at 247 MeV, compounded by the lower counting rates observed at this energy. The consistency between cross sections measured in different experiments was in general quite good. Inclusive particle production cross sections, as well as cross sections obtained from exclusive particle-particle correlations, were reproduced with relatively small deviations ($\sim$10–15 %). For measurements involving heavy fragments (inclusive and exclusive), systematic deviations between different experiments were somewhat larger. Apparent deviations between certain absolute cross sections were sometimes quite large ($\approx$15–40 %); these were traced to anomalous geometrical losses from the GT and did not affect multiplicity determinations. (The reduced geometrical efficiencies of the GT's were determined to be the same for inclusive and exclusive measurements, and were attributed to a small misalignment of the beam in one experiment.)

III. RESULTS FROM INCLUSIVE MEASUREMENTS

A. Inclusive studies-(H/He)

The nucleons and light-charged particles as observed by inclusive measurements are generated by a complex web of reaction mechanisms. In spite of this complexity, such measurements do provide signatures which allow mechanistic demarcations.[45–50] These demarcations are thought to be associated with a spectrum of time scales (albeit conceptually guided by crude clocks and fuzzy boundaries) which range from very fast prethermalization reactions to rather slow evaporationlike emissions from thermally equilibrated nuclei.

As shown in Fig. 2(a), it is not uncommon to observe signatures of both extremes. The angular distributions, shown in this figure, combine results from this study with previous measurements[51] to show two distinctive signatures. At the most forward angles, the strong forward peaking in the angular distributions for ^{1,2,3}H and ^{4}He suggests a prethermalization origin for these particles. For angles aft of 90° (c.m.) the distributions show a slightly backward peaked component; this signature is commonly associated with emission from thermally equilibrated sources (see, for example, Refs. 52 and 53).

The more limited measurements performed at 247 MeV do not allow similar displays, but the observed trends are the same. Similar trends are also exhibited by measurements performed for 196 MeV ^{40}Ar as shown in Fig. 2(b).[51] (These data have been corrected for contributions from carbon impurities on the targets by the method described in Ref. 21. The results given in Ref. 47 were not so corrected, and the forward peaking shown there is somewhat exaggerated.)

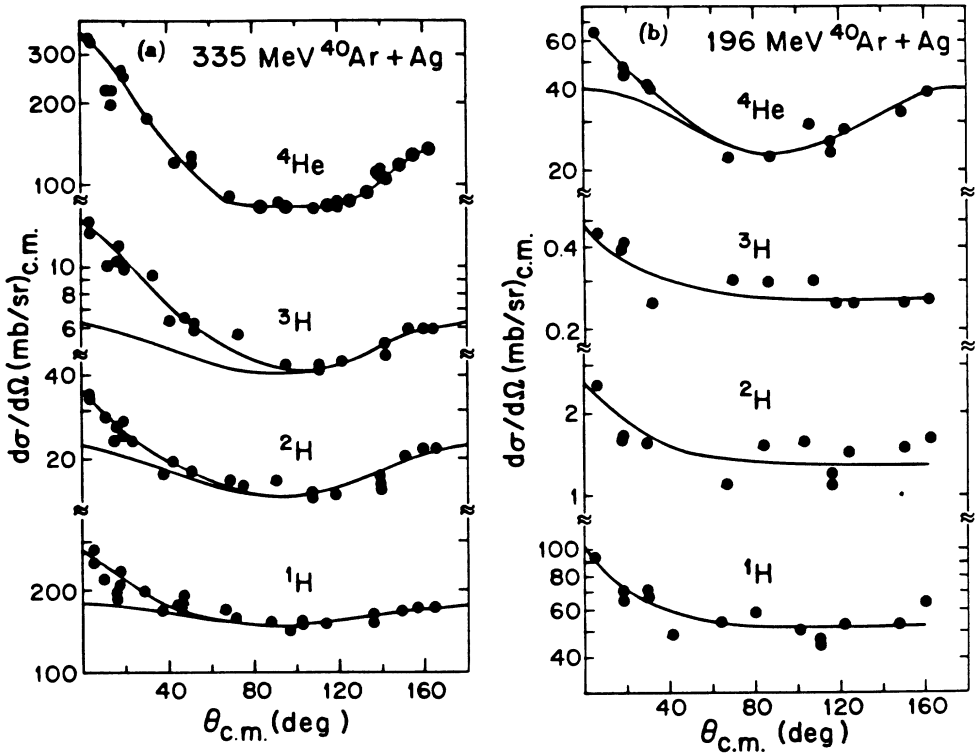

FIG. 2. (a) Measured angular distributions (c.m.) of the inclusive ^{1,2,3}H and ^{4}He particles for 337 MeV ^{40}Ar + ^{nat}Ag. (b) Same as (a) for 196 MeV ^{40}Ar + ^{nat}Ag (Ref. 51). Curves are drawn to guide the eye through the data points (upper) and symmetric about $\theta_{c.m.} = 90$ deg (lower).

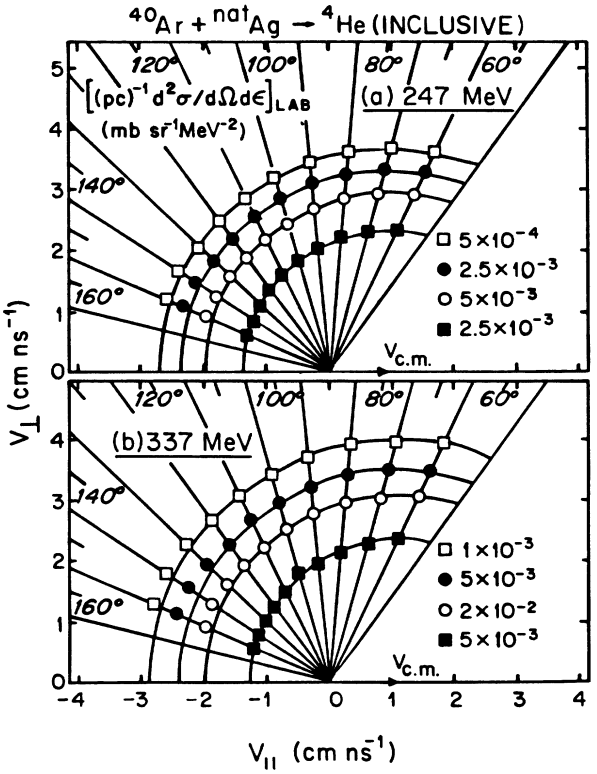

FIG. 3. Contour maps of the invariant cross section for inclusive ^{4}He emission. Maps are shown for 247 MeV (a) and 337 MeV (b) ^{40}Ar + ^{nat}Ag. The circular arcs are centered on the velocity of the center of mass ($V_{c.m.}$).

The major thrust of this paper concerns the evaporative components for ^{1,2,3}H and ^{4}He. It is therefore necessary to examine in detail the various signatures for evaporation. Figure 3 shows a pair of velocity contour maps of the invariant cross sections for ^{4}He production. These maps provide an overall picture of the reaction pattern for α particles detected in the backward hemisphere. Figures 3(a) and 3(b) show maps for ^{40}Ar beams of 247 and 337 MeV, respectively. The circular arcs centered on the c.m. velocity represent the data very well and therefore exclude the presence of prethermalization emission for a rather extensive angular range ($\theta_{lab} = 65° - 155°$). Particle emission from preequilibrium processes would result in strong deviations from these circles, especially

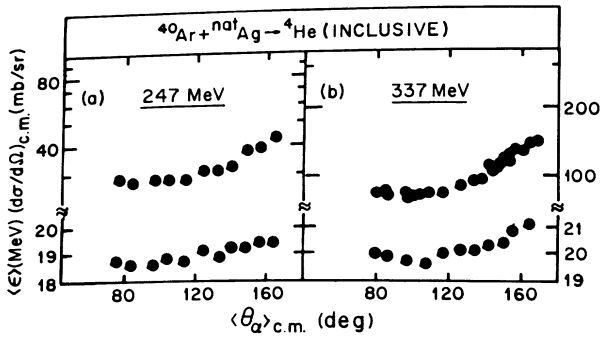

FIG. 4. Measured c.m. angular distributions (upper) and mean channel energies (lower) for inclusive ^{4}He particles. The ^{40}Ar beam energy was 247 MeV (a) and 337 MeV (b).

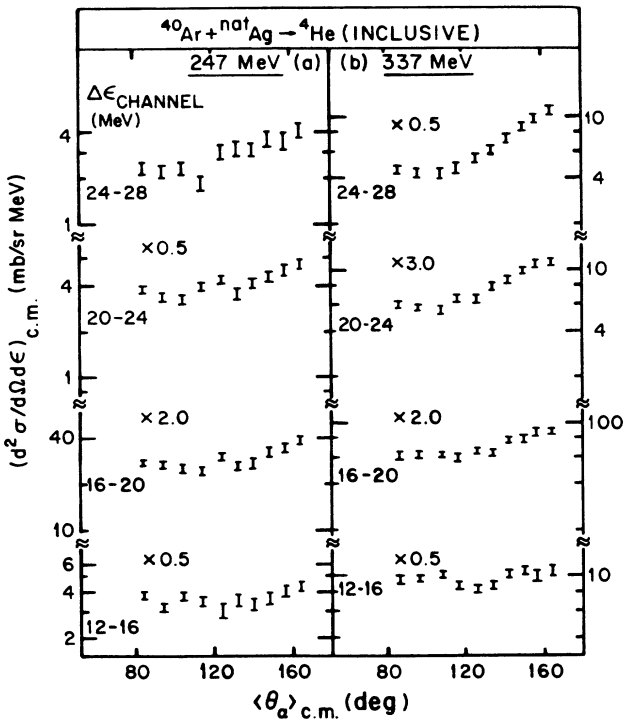

FIG. 5. Measured angular distributions (c.m.) of inclusive ^{4}He particles for various energy bins. Results are shown for the 247 MeV (a) and the 337 MeV (b) ^{40}Ar beams.

for the high velocities. This same feature is also apparent in the comparison of the forward and backward components of the angular distributions shown in Figs. 2(a) and 2(b). The small but noticeable deviations from the circles at the most backward angles can be attributed to angular anisotropies in evaporative decay that result from the spin of the emitters.[33,34]

The angular distributions shown in Figs. 4 and 5 give a more detailed view than the contour maps shown in Fig. 3. Figure 4 shows that both cross sections and mean energies increase with increasing emission angle. In addition Fig. 5 clarifies the increasing trend of angular anisotropy of the α particles with increasing energy. This feature serves as a further indication of the spin-driven nature of these evaporative emissions.[37] A final confirmation that particles detected in the backward hemisphere are derived from an evaporative mechanism is given by the energy spectra shown in Fig. 6. These energy spectra (transformed to the center of mass) for a number of detection angles are shown for ^{40}Ar beam energies of 247 and 337 MeV. Their Maxwellian shapes with low apparent temperatures and relatively small angular variations, reflect the characteristic features normally associated with evaporative processes. Also the most probable energies are very similar for the two bombarding energies, but higher spectral temperatures are evident in Figs. 6(b) for the 337 MeV beam. Detailed analyses of the various mechanisms which contribute to

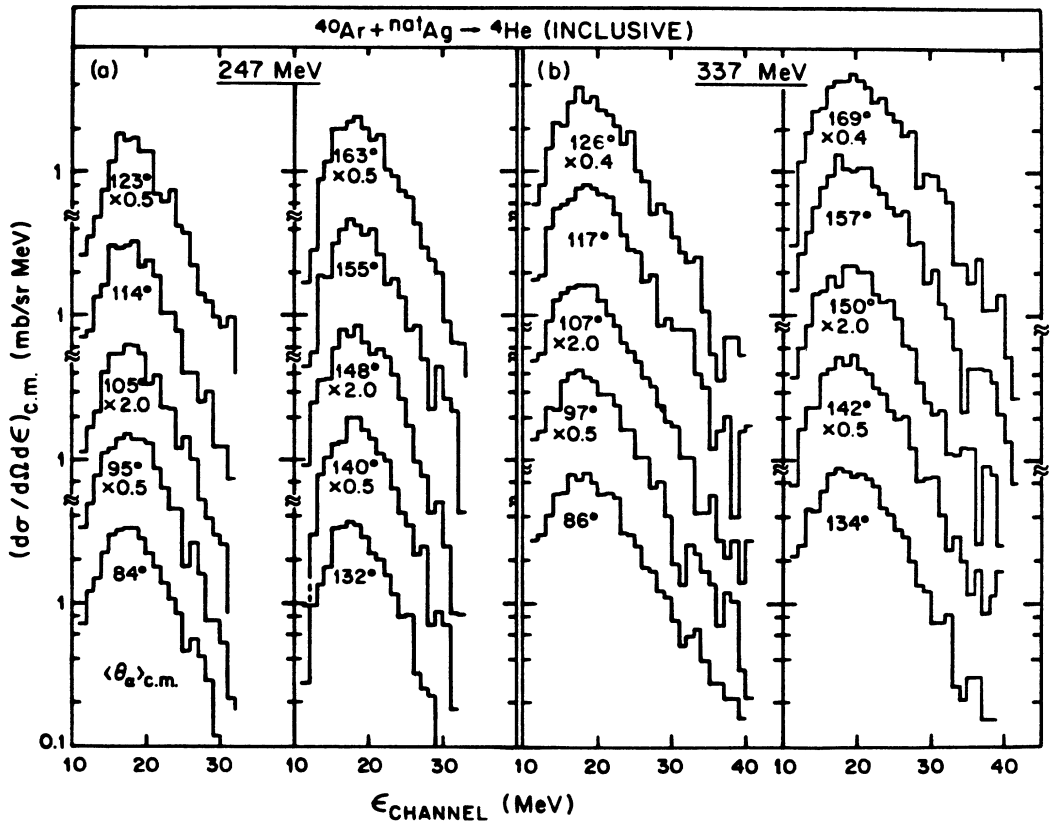

FIG. 6. Inclusive energy spectra for ^{4}He in the c.m. system. Spectra are shown for various c.m. angles for 247 MeV (a) and 337 MeV (b) ^{40}Ar beams.

TABLE I. Integrated charged particle cross sections (mb): evaporative components[a] for ^{40}Ar induced reactions.

E_{lab} (MeV)	Target[b]	^{1}H	^{2}H	^{3}H	^{4}He
185	^{116}Sn	453	9.1	2.5	194
196	^{nat}Ag	620	16.0	3.6	380
220	^{116}Sn	628	19.7	3.7	315
247	^{nat}Ag	834	38.2	11.3	421
271	^{116}Sn	956	57.4	17.7	555
337	^{nat}Ag	1870	167	56.0	1223
339	^{116}Sn	1697	155	56.6	1158

[a]$\sigma = 4\pi \int_{\pi/2}^{\pi} (d\sigma/d\Omega) \sin\theta_{c.m.} d\theta_{c.m.}$. The forward peaked component is not included in the integration. Absolute and relative uncertainties depend on the observed product and other factors in a rather complex way. For a detailed discussion see Appendix of Ref. 49. Roughly speaking, the relative uncertainties for ^{1}H and ^{4}He are $\approx 10\%$ and the absolute uncertainties are $\approx 20\%$.
[b]Results for the ^{116}Sn target are taken from Ref. 47. Those for 196 MeV ^{40}Ar + ^{nat}Ag are from Ref. 51.

these spectra are given in Sec. IV.

Angle integrated cross sections for ^{1}H and ^{4}He (evaporative components) agree well with results from Refs. 47 and 50 for the similar reaction system ^{40}Ar + ^{116}Sn. A summary of these cross sections is given in Table I. The agreement between absolute cross sections, as well as similarities for their energy dependences, reinforce our confidence in the reliability of the results.

B. Inclusive studies-(fussion fission/quasifission)

In order to exploit the full potential of light particle emission (n, ^{1,2,3}H, ^{4}He) as a mechanistic probe it is necessary to characterize the various mechanisms which contribute to their production. Good characterization not only allows a focused study of a particular mechanism, but also provides invaluable empirical information for input into model calculations. Since a major feature involves the association with fissionlike fragments, we first review the properties of these fragments.

TABLE II. Inclusive cross sections and spin zones for ER, QF, and FF products from ^{40}Ar + ^{nat}Ag.

Beam energy (MeV)	247	337
Excitation energy (MeV)[a]	128	194
σ_{ER} (mb)[b]	620±80	455±50
ER spin zone	0–68$\hbar$	0–70$\hbar$
σ_{FF} (mb)[c]	550±150	520±150
FF spin zone	68–94$\hbar$	70–103$\hbar$
σ_{QF} (mb)[c]	370±180	700±350
QF spin zone	94–108$\hbar$	103–133$\hbar$
σ_{QE} (mb)[b]	290±160	600±200
QE spin zone	108–123$\hbar$	133–157$\hbar$
$\sigma_{Reaction}$ (mb)[b]	2000	2270
l_{max}	123$\hbar$	157$\hbar$

[a]Total excitation energy of the hypothetical compound nucleus with no rotational energy subtracted.
[b]From Ref. 38. They report values for 236, 288, and 337 MeV.
[c]The values given here are from Ref. 38. Our cross section measurements at 35° are consistent with theirs, but the uncertainties relative to those for inclusive H and He (Table I) are only ±10%.

Detailed inclusive studies of the energy, charge, and angular distributions for the heavy fragments produced in the Ar + Ag reaction have been reported previously for several bombarding energies.[38,54–58] The fragments have been classified into four types: evaporation residues, fusion fission, quasifission, and quasielastic (QE), each associated with a separate range of entrance channel angular momentum (l_0). The measured cross sections are listed in Table II and a schematic illustration is shown in Fig. 7 of these different components of the cross section as a function of l_0. For this figure, a sharp cutoff in l_0 was assumed for the association of different processes with different spin regions. Two of these reaction types (FF and QF) are of particular interest in this study because the light charged particles associated with each provide a possibility for careful and detailed study of the properties of nuclei at quite high angular momentum.[3]

The experimental signatures employed here to identify FF and QF mechanisms are identical to the signatures previously reported.[38] Figures 8(a) and 8(b) show contour plots for heavy fragment detection by the GT in the $\Delta E - E$ and $Z - E$ planes for 337 MeV ^{40}Ar + ^{nat}Ag. Dashed and dot-dashed curves divide the fissionlike events into two groups as indicated. One group is consistent with symmetric fission of a compound nucleus of $Z \approx 64$ (dashed curve); the other corresponds to products centered about the projectile Z of 18 and were assigned to the QF mechanism. The Z values in Fig. 8(b) were generated from Fig. 8(a) by using the known thickness of the ΔE detector along with the SPAR code.[59] This code provides for transformation from $\Delta E/\Delta X$ and E (after correction for pulse-height defect[42]) to a certain Z value. The charge and energy distributions of the FF and QF products at 35° (from ^{40}Ar of both 247 and 337 MeV) were very similar. Quasielastic and elastic reaction products were also observed at 35° for 247 MeV ^{40}Ar; these were absent from the results for 337 MeV because of the smaller grazing angle [$\theta_{lab} = 35°$ (22°) for 247 (337) MeV].

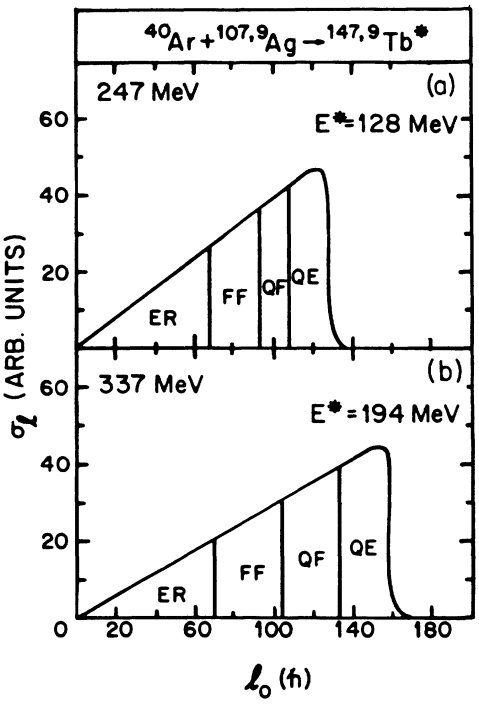

FIG. 7. A schematic illustration of the cross section as a function of entrance channel angular momentum (l_0) (a) 247 MeV ^{40}Ar (b) 337 MeV ^{40}Ar. Experimental cross sections were obtained from Ref. 38 and this work. Spin zones are indicated for ER production and for the fissionlike reactions, FF and QF.

IV. RESULTS FROM FRAGMENT PARTICLE CORRELATIONS

A. Technique for separation into composite-nucleus emission and fragment emission

In Sec. III the well-known symmetry properties of evaporative emission were used to demonstrate a rather clear distinction between the evaporation and prethermalization particles as detected in the backward and forward hemispheres, respectively. It was noted that even for evaporative particles there are contributions from many possible emitters derived from several mechanisms. In order to sort out these separate contributions, we use the well-established procedure[37] of considering two types of evaporative emission (CE and FE). This procedure employs the spectra from fragment particle coincidence measurements and exploits the different kinematic shifts associated with FF and QF triggers.[30,31,40] The key to this analysis is, of course, the very different laboratory angular dependence expected for the charged particles from each source as dictated both by kinematics and by the source characteristics.

A necessary ingredient for good kinematic analysis of the particle emission is the consideration of several emitter types and the distributions of their properties (Z, lab velocity, etc.). It is necessary to make reaction-simulation calculations that fold together the various distributions in velocity, mass, charge, and angular momen-

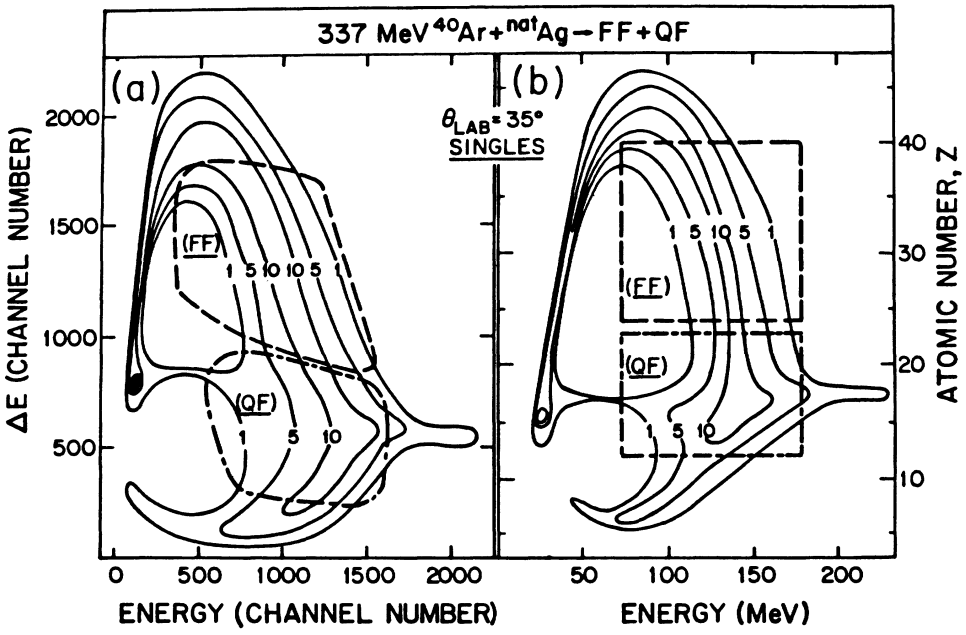

FIG. 8. Contour maps of the QF and FF fragments for 337 MeV ^{40}Ar + ^{nat}Ag. The $Z-E$ map (b) was generated from the $\Delta E-E$ map (a) by using the SPAR code (Ref. 59). The dot-dashed and dashed curves indicate the fragments characterized as QF and FF, respectively. Results for 247 MeV Ar + Ag are similar.

tum of the heavy fragments. In addition, it is desirable to impose restrictions on the calculations which are identical to those of the experiment such as detection geometry, energy thresholds, and detector size. To accommodate these requirements and to gain statistical significance in the analysis, a weighted Monte Carlo reaction simulation code (GANES) has been developed.[37]

The basic objective of the GANES program is the simulation of evaporative processes leading to particle emission in specified laboratory directions. The code employs semiclassical statistical theory[33,34] to calculate evaporation spectra for various emitting nuclei (e.g., composite nuclei, FF or QF fragments). Angular correlations corresponding to several possible coincidence requirements are also addressed by the code. The Monte Carlo reaction simulation code takes account of the entrance-channel spin distribution, heavy fragment mass and energy distributions, and the kinematic transformations associated with each type of emitting nucleus. The energy and angular distributions provided by the code for a given ensemble of moving emitters, serve as a basis for the analysis. By normalizing the simulated spectra to those experimentally observed, integrated multiplicities can be determined for each of the major emission sources.

Before discussing results and details of this analysis, it is instructive to consider a few points associated with the simulation so as to clarify the origin of some of the important model parameters. It is evident that the fundamental task of the code is the repetitive vector summation of emitter and emission velocities, after full consideration of the physical ingredients that control the intrinsic evaporation spectra. Among these are barrier magnitude, penetration probability, orientation of emitter spin, recoil effects, and the angular, energy, and mass (or charge) distributions of the fragments.

The energy, mass, and angular distributions of the fragments were obtained from inclusive measurements performed in this study as well as from previous studies.[38,54] The intrinsic evaporation spectra of the particles were derived from recent extensions of evaporation theory.[37] Fermi gas, spin-dependent level densities were used with entrance channel angular momenta inferred from cross section measurements (using the sharp cutoff approximation, see Table II). Transmission coefficients were calculated with the Hill-Wheeler formula.[60] The degree of spin alignment with respect to the reaction plane (defined by the beam and fragment direction) was determined from the standard theory of fission fragment angular distributions.[61–64] Angular momentum transfer to the fragments was computed by assuming rigid rotation at the scission configuration. Particle evaporation barriers were determined from systematics[65] for emission from the fragments. For emission from the composite system, evaporation barriers were also calculated for deformed emitters as described in Ref. 37.

Charged particle spectra were calculated for trigger configurations identical to those of the experiment and normalized to experimental data to provide multiplicities for FF and QF triggers. To illustrate the nature of this normalization, the results for FF and QF triggers are presented separately below.

B. Coincidences between H or He and FF trigger fragments

Experimental and calculated spectra for α particles triggered by FF fragments are shown in Figs. 9(a) and 9(b) for 337 MeV ^{40}Ar and Figs. 10(a) and 10(b) for 247 MeV ^{40}Ar. Figures 9(a) and 10(a) show results for in-plane trigger detection and Figs. 9(b) and 10(b) for out-of-plane trigger detection. The vector diagrams in these figures provide a quick and straight-forward orientation to expected kinematic patterns and serve as a useful pedagogic guide. Vector triangles in Figs. 9 and 10 show three components representing average velocities for the composite system, the detected and undetected fragments. The vector for the composite nucleus points along the beam direction while the vector for the detected fragment points in the direction of the GT trigger. The vector for the undetected fragment is located in the quadrant opposite to that of the detected fragment as fixed by linear momentum conservation in a two body reaction. Centered on the tips of these fragment vectors are circles with radii that represent the average ^{4}He velocities calculated for CE (solid circle) and FE (dashed circles). In order to keep the reaction plane horizontal, the diagrams for out-of-plane (oop) trigger detection have been rotated by 90°. (The velocity vector for undetected fragments is not shown in these oop diagrams.)

On the vector diagrams, the particle detector positions are numbered to show their correspondence with the spectra. Detector thresholds are indicated with bars. It is quite clear from these diagrams that the angular dependence of the average laboratory velocities for ^{4}He emission are very different for fragment and composite emission. In addition, the spectral intensities tend to follow the magnitudes of the laboratory velocities due to the Jacobian factors. Specifically, if one focuses on the vector diagram of Fig. 9(a) it can be seen that positions 2 and 3 emphasize kinematic shifts associated with emission from the detected fragments while positions 9 and 10 are most sensitive to analogous shifts for emission from the undetected fragments. Similarly, positions 5 and 6 accentuate emission from the composite nucleus; in fact, they can be expected to provide good separation between FE and CE since FE essentially falls below the threshold for these detectors.

An inspection of Fig. 9(b) also reveals that separation between CE and FE is provided at all angles by the special kinematics of out-of-plane trigger detection. Differences between the two types of emission are particularly emphasized for positions 1, 2, and 3. The vector diagrams of Fig. 10 for 247 MeV ^{40}Ar are quite similar to those of Fig. 9 for 337 MeV ^{40}Ar. In describing these vector diagrams, the important regions which allow good separation between FE and CE were pointed out above. It should be emphasized however, that one of the more powerful aspects of these diagrams is the view it gives of the overall trends of the kinematic patterns, as one surveys the complete angular range of the measurements.

The histograms in Figs. 9 and 10 show measured laboratory spectra of the α particles. The in-plane spectra

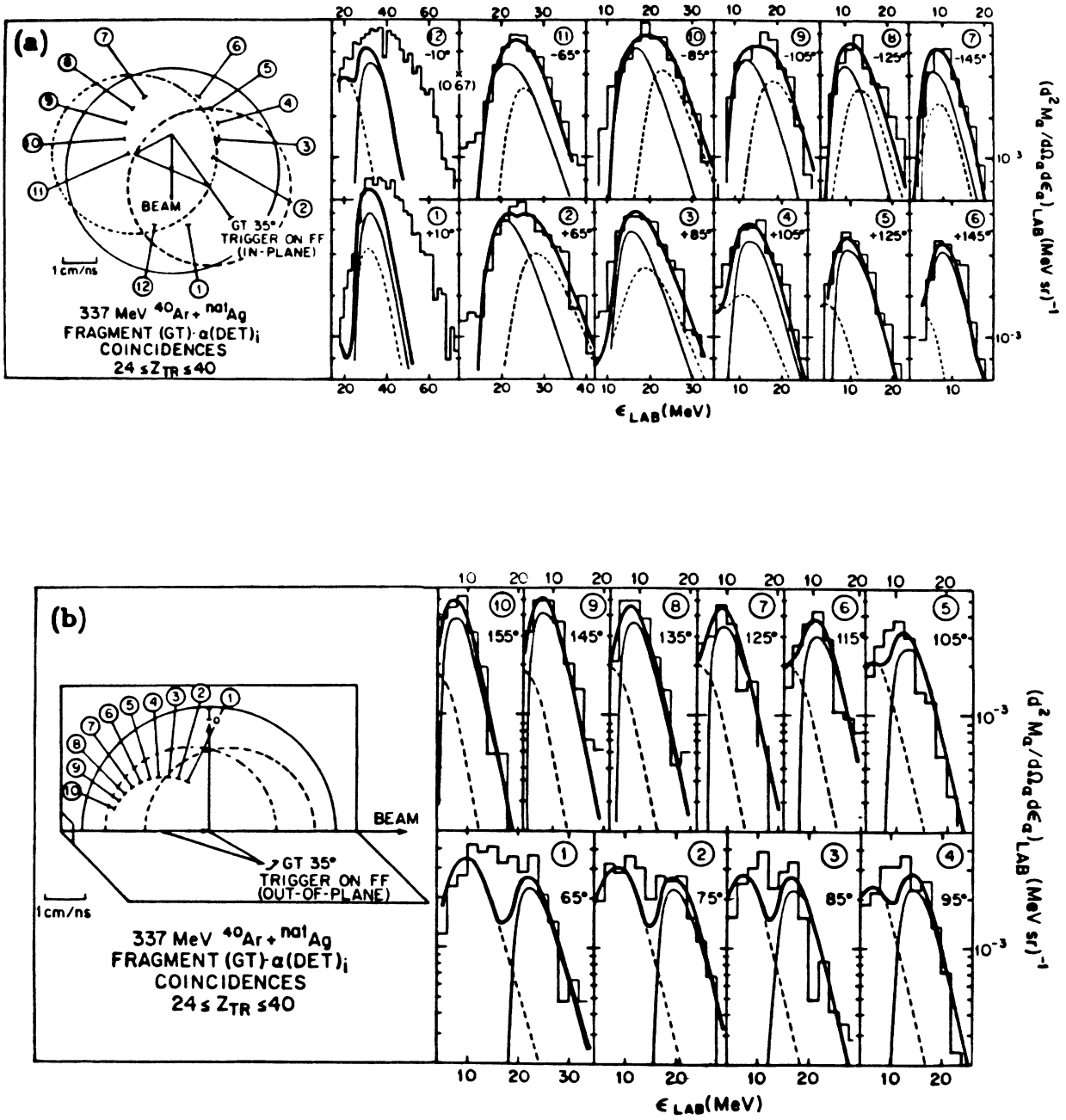

FIG. 9. Coincidence spectra for ^{4}He from the reaction 337 MeV ^{40}Ar + ^{nat}Ag. (a) In-plane FF trigger detection. (b) Out-of-plane FF trigger detection. The dashed and light solid curves represent the simulated contributions from FE and CE, respectively. The dark solid curves indicate the sum of these contributions. Detectors are numbered to correspond to the positions indicated on the vector diagrams. Average velocities for FE and CE are denoted by circles on the vector diagrams (dashed circles and solid circles for FE and CE, respectively).

[Figs. 9(a) and 10(a)] are dominated by a single peak which includes the separate contributions of both FE and CE processes. The broader out-of-plane spectra [Figs. 9(b) and 10(b)] show a double humped structure. These differences in the particle spectra (obtained in the same detector, but for in-plane and out-of-plane triggers) are mainly due to the reaction kinematics for FE and to angular momentum effects for CE.

Superimposed on these histograms are curves representing calculated α-particle spectra for FE (dashed curves), CE (light solid curves), and their sum (dark solid curves). Input parameters for these calculated spectra are discussed in Sec. V below. Our concern here is mainly with the kinematics and the normalizations. The normalization procedure can be illustrated for Fig. 9. An upper limit for FE was assigned, essentially by reference

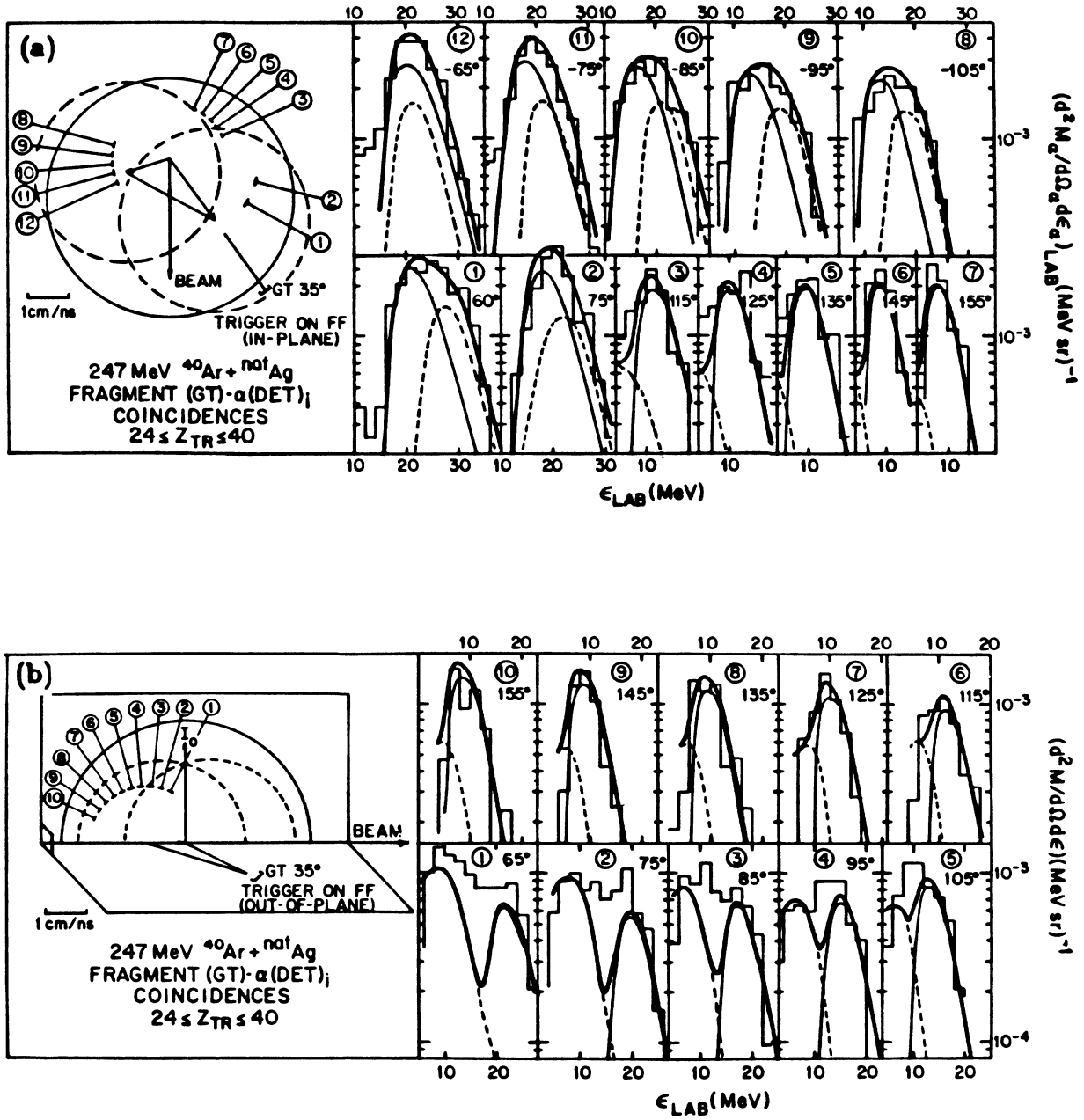

FIG. 10. Same as Fig. 9 for 247 MeV ^{40}Ar + ^{nat}Ag.

to positions 2, 9, and 10 of Fig. 9(a) and 1, 2, and 3 of Fig. 9(b). Similarly, an upper limit for CE was assigned by reference to positions 5 and 6 of Fig. 9(a) or 1 and 2 of Fig. 9(b). This choice was dictated by the fact that these detectors are located in angular regions where FE and CE are best separated. Further refinements were made by small adjustments of these intensities to assure general acceptability of the fits at all angles. It should be stressed here that this process of assigning FE and CE contributions is a very stringent one. A single normalization of the FE or CE contribution to an experimental spectrum at one angle, fixes the magnitudes of the simulated spectra at all other angles. Consequently, the fitting procedure not only demands that the constraints imposed by kinematics be met, but also that the angular distributions be correctly represented as derived from the Jacobians and spin effects.

The dark solid curves in Figs. 9 and 10 show that the experimental data are very well represented by the sum of the two evaporative components (FE and CE). It is especially important to point out that the simultaneous representation of both the in-plane and out-of-plane data provides information concerning the out-of-plane angular distribution of these emitted particles. These angular dis-

tributions, which are needed for accurate multiplicity determinations, also provide important clues to the roles of spin, temperature, and shape (or size) of the emitters.

In spite of the general acceptability of the fits, there are some deviations which point to the existence of processes separate from CE and FE. In Fig. 9(a) the two most forward positions (1 and 12) show an excess of high-energy particles. These α particles are ascribed to prethermalization emission (PTE) since they are more energetic than either of the two evaporative sources. Figures 9 and 10 also show deviations between experimental and simulated spectra that appear as a small surplus of particles with energies intermediate between those for FE and CE. These deviations, which are most prominent for out-of-plane trigger detection [Figs. 9(b) and 10(b) positions 1–4], can be attributed to near-scission emission (NSE).[28,31,66,67] The NSE process is expected to be favored at angles of $\approx 90°$ to the separation axis of the fragments. The surplus of these particles for α detection outside the reaction plane [particularly visible for 247 MeV ^{40}Ar, positions 1–5 in Fig. 10(b)] seems at first to be a different signature from that previously reported for the NSE process.[67] However, in this case our energy threshold for ^{4}He limits the sensitivity to low-energy particles at very large angles. Nevertheless we do see very small, low-energy excesses in the reaction plane at angles $\approx 90°$ to the separation axis [see for example position 12 in Fig. 9(a) and position 4 of Fig. 10(a)].

The integrated ^{4}He multiplicities derived from the fits to the experimental spectra for CE and FE, respectively, are 0.300 and 0.276 for the 337 MeV ^{40}Ar beam and 0.090 and 0.072 for the 247 MeV ^{40}Ar beam. Statistical uncertainties associated with these values are $\approx 5\%$ for 337 MeV and $\approx 10\%$ for 247 MeV. These multiplicity values are discussed later but are presented here to emphasize the fact that a large fraction of the total α-particle multiplicity is derived from particles emitted by the composite system. This is a very striking result because the composite systems which emit these particles have a root-mean-square (rms) spin value which exceeds that for which the calculated fission barrier goes to zero.[68]

Figures 11(a) and 11(b) present a sample of the fragment-particle correlation results for ^{1}H. (The statistical significance was quite poor for coincidence spectra obtained for ^{2,3}H along with heavy fragments and they are not considered here.) The kinematic situation for ^{1}H emission can be easily inferred from the vector diagrams for ^{4}He in Figs. 9 and 10. Since the mean proton velocities exceed those for ^{4}He, one can mentally expand the radii of the circles in these figures. It is important to point out that, except for the much smaller kinematic shifts, the kinematic patterns are qualitatively the same, and therefore the criteria for assigning FE and CE contributions for these particles are parallel to those used for ^{4}He.

These two pairs of spectra shown in Fig. 11 give results from the two available angles which impose the maximum kinematic constraints for FE and CE separation (60°, triggered in-plane and out-of-plane). These angles are very close to those for position 1 in Figs. 10(a) and

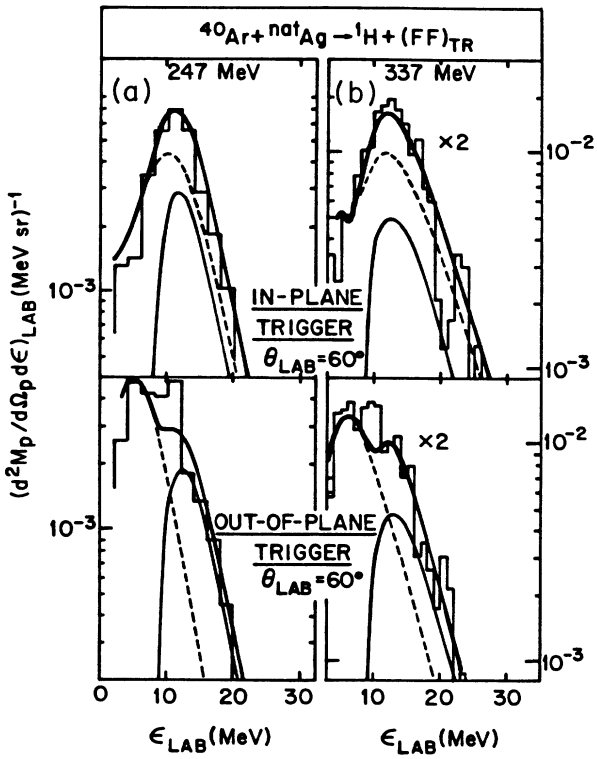

FIG. 11. (a) Coincidence spectra for ^{1}H from the reaction 337 MeV ^{40}Ar + ^{nat}Ag ($S-3$ with FE trigger fragments). Spectra are shown for the two available angles which impose the maximum kinematic constraint for the separation of FE (dashed curve) and CE (light solid curve). The sum of the FE and CE contributions are represented by the dark solid curves. (b) Same as (a) for the 247 MeV ^{40}Ar beam.

10(b); the circles (shown there for ^{4}He) would have larger radii if they were drawn for ^{1}H. Following the previous notation used for ^{4}He, the curves in Figs. 11 represent calculated proton spectra for FE (dashed), CE (light solid), and their sum (dark solid). These figures clearly demonstrate that the two-process description is quite adequate for the protons. The deviations of the data from these fits are qualitatively similar to those discussed above for the α particles. Consequently, the same associations can be made for the unaccounted-for portions of the experimental spectra (i.e., NSE in Fig. 11). Integrated multiplicities, given in Table III below, indicate that the composite system is an important source for the protons, but not dominant as it was for the alpha. The same input parameters have been used to describe the emission sources for ^{1}H in Fig. 11 and for ^{4}He in Figs. 9 and 10. These parameters are discussed in Sec. V below. The observed differences between the multiplicities for ^{4}He and ^{1}H as well as the H/He ratio for FE and CE are also quite interesting.

Discussion of the mechanistic implications of these results is deferred to Sec. V to allow presentation of some additional results.

TABLE III. Fragment-particle coincidences (multiplicities M and cross sections σ).[a-d]

	M_{CE}	σ_{CE} (mb)	M_{FE}	σ_{FE} (mb)	$\sigma_{CE}+\sigma_{FE}$ (mb)
			337 MeV ^{40}Ar + Ag.		
ER$-\alpha$	1.4 $\pm$0.4[b]	637$\pm$177[b]	0	0	637$\pm$177
FF$-\alpha$	0.300$\pm$0.030	156$\pm$23	0.276$\pm$0.028	144$\pm$22	300$\pm$32
QF$-\alpha$	0.137$\pm$0.014	96$\pm$14	0.273$\pm$0.027[c]	191$\pm$29[c]	286$\pm$32
ER$-p$	2.1 $\pm$0.6[b]	957$\pm$277[b]	0	0	957$\pm$277
FF$-p$	0.254$\pm$0.025	132$\pm$20	0.642$\pm$0.064	334$\pm$50	466$\pm$54
QF$-p$	0.184$\pm$0.018	129$\pm$19	0.454$\pm$0.045[c]	318$\pm$48[c]	447$\pm$52
			247 MeV ^{40}Ar + Ag		
ER$-\alpha$	0.501$\pm$0.101[b]	311$\pm$50[b]	0	0	311$\pm$50
FF$-\alpha$	0.090$\pm$0.014	50$\pm$10	0.072$\pm$0.01	40$\pm$8	90$\pm$13
QF$-\alpha$	0.018$\pm$0.003	7$\pm$1	0.035$\pm$0.005[c]	13$\pm$3[c]	20$\pm$3
ER$-p$	1.02 $\pm$0.20[b]	630$\pm$88[b]	0	0	630$\pm$88
FF$-p$	0.10 $\pm$0.01	55$\pm$11	0.208$\pm$0.02	114$\pm$12	169$\pm$17
QF$-p$	0.027$\pm$0.005	10$\pm$2	0.067$\pm$0.013[c]	25$\pm$5[c]	35$\pm$6

[a]M denotes particle multiplicity; σ denotes the cross section for ER or FF or QF; $\sigma_{CE}=M_{CE}\sigma$ ($\sigma_{FE}=M_{FE}\sigma$), i.e., the angle integrated cross section for particles of a given type. Estimated uncertainties for the multiplicities for FF and QF are generally $\approx$10%. (For QF at 247 MeV they are $\approx$15%.) Relative uncertainties for σ_{FF} and σ_{QF} are $\pm$10%. Both of these components have been integrated (with a $1/\sin\theta$ angular distribution) (Refs. 38 and 54). The absolute uncertainty in this procedure is given by the errors assigned to σ_{QE} in Table I.

[b]For determination of ER cross sections the contributions for FF and QF (targetlike only) were subtracted from the evaporative singles observed at backward angles. An additional error was assigned to account for possible contributions from partially damped reactions. This error was taken to be $\sigma_{QE}(1/2)(M_{FE}+M_{CE})_{QF}$. These errors include those for deviations from $1/\sin\theta$ angular distributions for FF and QF.

[c]The multiplicities for the projectilelike fragments from QF (not included above) are 0.13 and 0.13 for ^{4}He and ^{1}H (337 MeV).

[d]The data used here for ^{40}Ar + ^{nat}Ag$\rightarrow^4$He include those used for Ref. 3 along with two additional experiments with better statistics, lower thresholds and much more angular coverage in-plane, as well as out-of-plane. The analysis here invokes a deformed emitter to address the out-of-plane data (not available for Ref. 3). The qualitative conclusions of Ref. 3 are not changed, but for ^{4}He some of the quantitative multiplicity values should be updated by this work.

C. Coincidences between H or He and QF trigger fragments

The coincidence spectra shown in Fig. 12 for ^{4}He are associated with QF trigger fragments, identified as in Ref. 38 with $12 \leq Z \leq 23$. Figures 12(a) and 12(b) show results for in-plane and out-of-plane trigger detection respectively. The results for 247 MeV ^{40}Ar are qualitatively similar; however, the cross sections are much smaller, as indicated in Table III. For orientation, it is again useful to study the vector diagrams in Figs. 12(a) and 12(b), and to assimilate the expected kinematic patterns for FE and CE. The velocity vector for the detected fragments is, of course, fixed by the GT angle in the same direction as shown for the FF trigger. However, the direction of the undetected fragments is quite different for QF due to the larger velocities and smaller masses of the detected QF fragments. Focusing attention on Fig. 12(a), it is apparent that positions 2 and 3 should provide clear signatures for emissions from the detected and undetected fragments as well as from the composite system. Note the large differences in the expected mean velocities. It is also of particular interest to point out that the strong kinematic focusing of FE from the detected fragment provides a rather clear angular region for CE identification (positions 4, 5, and 6). This is illustrated very well by the rapid change in ^{4}He intensity calculated for emission from the trigger fragment as the particle detection angle increases (see for example detectors 2 and 3). A survey of the other angles shows that positions 4 and 5 should emphasize the kinematic shifts associated with CE while the mirror image detectors (positions 8 and 9) are expected to accentuate emission from the undetected fragments. An inspection of the vector diagram for the out-of-plane configuration indicates that here a clear separation between FE and CE cannot be expected. Nevertheless, these detectors give strong constraints on the proper representation of the ^{4}He angular distributions with respect to the emitter spin. The kinematic patterns from similar vector diagrams for ^{1}H emission have very similar trends, albeit with less pronounced kinematic shifts.

The histograms in Fig. 12 give experimentally observed spectra; the smooth curves give simulations for α-particle emission at the same angles. These experimental spectra show clear signatures for fragment emission as exemplified by the detector pair at positions 2 and 11, symmetrically fixed at $\pm$65° (with respect to the beam). An initial normalization was accomplished via the spectra shown in Fig. 12(a). The low-energy peak at position 2 was identified with emission from the undetected fragment and served as the basis for fixing the contributions from this source at all other angles. Similarly the high-energy tail (also for position 2) was identified with emission from the detected fragment. Contributions from CE were assigned essentially by reference to positions 4 and 5, following the FE assignment for the undetected frag-

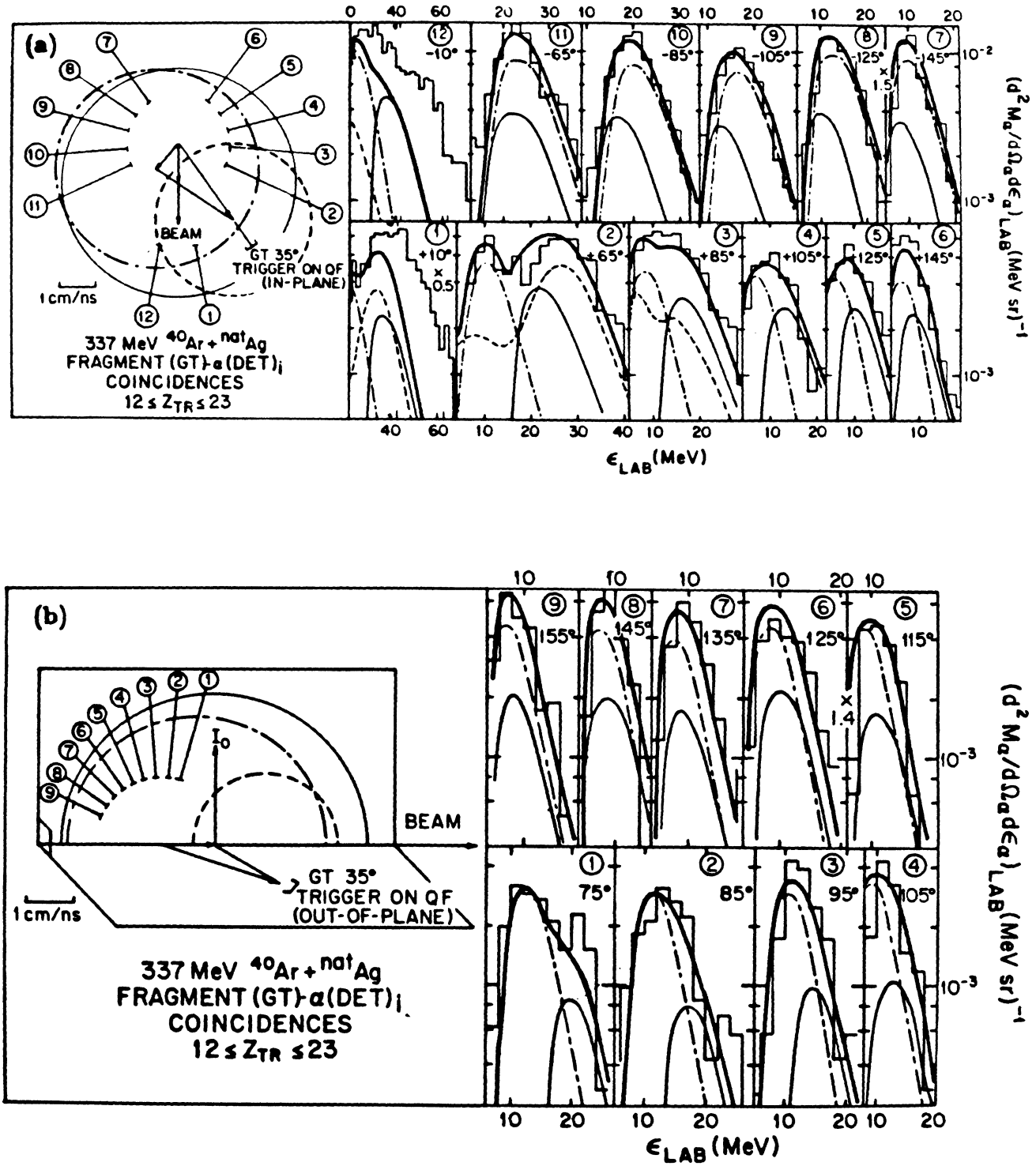

FIG. 12. Same as Fig. 9 for ^{4}He from the reaction 337 MeV ^{40}Ar + ^{nat}Ag. (a) In-plane QF trigger detection. (b) Out-of-plane QF trigger detection.

ment. To improve the overall quality of fit, final refinements were then made. Out-of-plane results, shown in Fig. 12(b), do not impose any important additional kinematic constraints, but they do show that the angular distribution is correctly accounted for.

Figure 12 gives a clear demonstration that the observed ^{4}He coincidence cross sections can be largely accounted for by FE and CE. The different patterns shown in Fig. 12 compared to Fig. 9 show a distinct change in the relative importance of CE vs FE. Also visibly absent for the QF trigger, are the excess emissions at intermediate energy that were previously identified for FF triggers as near scission emission. We can also use these results to search for the shadowing phenomenon[66,69–71] reported

by the Heidelberg group. Figure 13 shows a subset of these coincidence spectra that focuses on the angular dependence of ^{4}He emission from the heavy undetected fragment. This dependence is well described by the simulation for positions 1 and 2 in Fig. 13 as well as for positions 8–11 in Fig. 12(a). However, there is a distinct deficit in the data for Fig. 13 position 4, i.e., for the SST at 60° only 25° from the detected fragment. Similar, but much more detailed observations have been reported previously.[66,69–71] which have been attributed to shadowing. If emission occurs from a target-like fragment which is still rather close to its scission configuration, then coulomb deflection by the newly born trigger fragment could result in a depletion of particles in directions near to that of the detected fragment.

Coincidence spectra for ^{1}H with QF fragments are shown in Fig. 14. One pair of spectra is shown for reactions of 337 MeV ^{40}Ar to highlight the fact that a preponderance of the protons is derived from the fragments. The spectra are from the two available angles which impose the maximum kinematic constraints for FE and CE (60° triggered in plane and out-of-plane). The dark solid curves, which denote the sum of FE and CE, represent the data very well; they employ the same parameters to describe the ^{1}H emission (Fig. 14) and the ^{4}He emission (Fig. 12). The close comparisons demonstrate the similarity between ^{4}He and ^{1}H emission for QF fragments. In spite of this overall similarity, it is interesting that the shadowing phenomenon observed for ^{4}He is not evident in these results for ^{1}H. Similarities and differences between ^{1}H and ^{4}He emission are discussed further in the next section.

V. MECHANISTIC IMPLICATIONS OF FRAGMENT-PARTICLE CORRELATIONS

A. An overview of sources and trends

In the preceding section, the kinematic aspects of ^{1}H and ^{4}He emission in association with FF and QF fragments were considered. It was shown, that the combined evaporative emissions from the fragments and the composite system account for most of the fragment-particle coincidence cross sections. In addition, a clear distinction between the separate contributions of FE and CE was made, and signatures for three other phenomena (NSE, PTE, and shadowing) were noted. A more detailed investigation of the implications of these results is undertaken in this section.

In Table III the measured cross sections and multiplicities are summarized for protons and α particles for 337 and 247 MeV ^{40}Ar + ^{nat}Ag. For ^{1}H and ^{4}He we have determined these angle-integrated particle multiplicities at a trigger angle of 35° for FF or QF. We then assume that the particle multiplicity (for FF or QF) does not depend on trigger angle and thus assign an angle integrated cross section as the product of trigger-fragment cross section times the multiplicity. Cross sections for ^{1}H or ^{4}He from the evaporation residues are determined by subtracting the cross sections for evaporative ^{4}He (and ^{1}H) in association with FF and QF from the total inclusive evaporative cross sections (Table I). The remainder ($\approx 1/2$ for 337 MeV ^{40}Ar and $\approx 3/4$ for 247 MeV ^{40}Ar) is assigned to the ER's. Average particle multiplicity for the ER's is then obtained by dividing by the ER cross section (Table II).

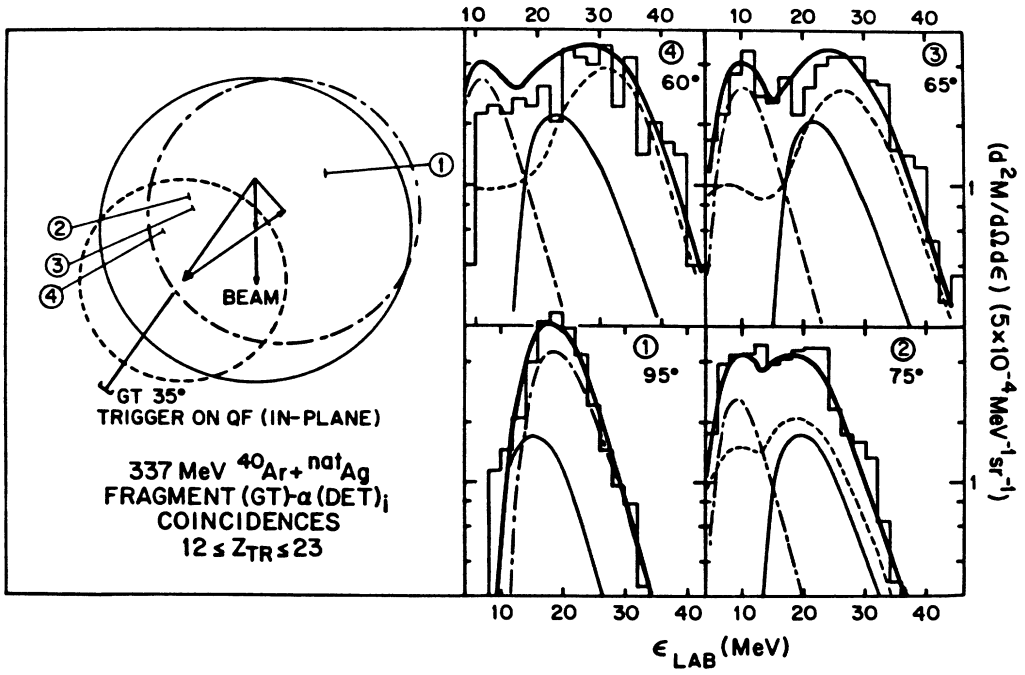

FIG. 13. Same as Fig. 9(a) but with spectra from several different angles.

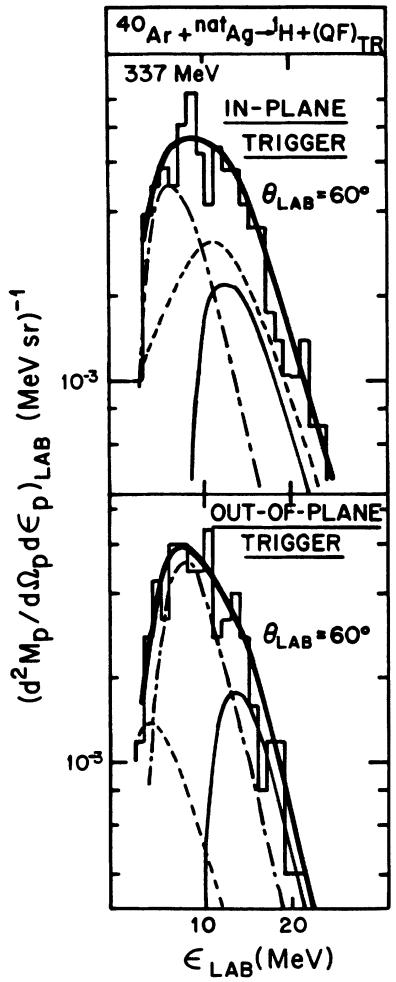

FIG. 14. Same as Fig. 11 for ^{1}H from the reaction 337 MeV ^{40}Ar + ^{nat}Ag ($S-3$ with QF trigger fragments).

Several major features of the reactions are illustrated by the data in Table III: (1) The CE processes for both FF and QF have substantial multiplicities. (2) Multiplicities for both ^{1}H and ^{4}He are much smaller for fissionlike reactions (FF and QF) than for ER production. (3) Multiplicities for CE emission decrease substantially for QF compared to FF reactions. Let us consider these points individually.

(1) A substantial cross section (for ^{1}H and ^{4}He) is associated with reactions which produce fissionlike fragments and a sizeable fraction of these particles result from CE. The surprisingly large CE multiplicities as well as their rapid increase with energy are particularly striking. These seemingly energy-equilibrated composite systems are calculated to have vanishing fission barriers for $J \geq 80\hbar$;[68,72,73] hence they are expected to decay immediately via the fission channel.[74] It is clearly difficult to reconcile these observations of substantial CE emission with the notion that phase space alone determines the final formation probabilities of the reaction products. This stance is commonly used in statistical models.[33,75] The suggestion has been made that in addition to phase space it is the dynamical aspects of emission (i.e., the intrinsic rates), which control the CE multiplicities.[3–5,46,47,50,76–80] This notion can provide a qualitative explanation of these results. Nuclear distortion toward fission proceeds through collective motions which move large numbers of nucleons toward the scission point. If this motion is slow compared to the intrinsic time for particle evaporation, (i.e., thermalization and subsequent emission) then substantial prescission emission can be expected. Indeed, theoretical calculations that incorporate the known effects of nuclear dissipation do indicate several important dynamical aspects that can affect particle decay during the fissionlike decay motion. (a) The fission probability is suppressed (relative to the calculated Bohr-Wheeler value[74]) due to the superposition of the Brownian nature of the particle motions and the collective flow toward the saddle point.[78] (b) There is a finite time delay involved in the buildup of the fission probability at the saddle point.[77–80] This time delay can enhance evaporation-like, prescission emission. (c) In addition, the model of Hofmann and Nix[81] has indicated that particle emission might even occur during the somewhat later stage of descent from the saddle point to the scission point.

(2) For a given bombarding energy, the particle multiplicities associated with CE decrease with increasing angular momentum. This effect is particularly dramatized in Table III for the two angular momentum zones corresponding to the ER and FF reactions (^{1}H and ^{4}He show FF/ER multiplicity ratios $\approx 1/8$ and $\approx 1/4$, respectively, for the 247 and 337 MeV ^{40}Ar beams). The rapid decrease of these CE multiplicities dramatizes the role of competition from fissionlike processes at higher angular momenta. It is also interesting to point out that the CE multiplicities for these two spin zones change more rapidly for ^{1}H than for ^{4}He. In addition, the H/He multiplicity ratios for CE are much larger for the ER reactions of lower spin zone. These observations are consistent with the expectation that increasing spin causes an increase in α-particle evaporation compared to proton evaporation due to their relative powers for angular momentum removal.

(3) A comparison of the QF and FF multiplicities indicates that CE contributions for QF are substantially less than those for FF. These results are probably related to the shorter lifetimes and the lower excitation energies of the composite nuclei produced in QF compared to FF reactions. The forward peaked angular distribution, often observed for projectilelike fragments, suggests that scission occurs before the complex can complete a rotation. The angular symmetry for FF fragments suggests more extensive rotation and hence a longer lifetime for the composite nucleus. However, it is interesting that for 337 MeV ^{40}Ar (247 MeV ^{40}Ar) this multiplicity decrease for CE is only $\approx 1/2$ ($\approx 1/4$) from FF to QF; one might conclude that the lifetimes for FF and QF differ by similar factors. Since the composite system lives for less than one rotation period for QF, it would seem that it lives only slightly more than one rotation period for FF. This result implies that fusion fission for this hot, rapidly rotating system does not require a much longer time period than quasifission.

B. Energy and angular distributions of particles evaporated from the composite nuclei

The combined results of these particle multiplicities and their energy and angular distributions are consistent with a picture of statistical evaporation modulated by the dynamics of fissionlike decay. If such a picture is indeed operative, the characteristics of the evaporationlike particles are governed by the statistical properties of the emitting nuclei. Hence, the properties of the particles provide a useful route for the investigation of the emitters. In the discussion of Figs. 9–14 above, we stressed the use of the kinematic shifts and angular symmetries to obtain the separate contributions of CE and FE. In addition, these experimental data put some very specific constraints on the properties of the composite-nucleus emitters. Root-mean-square spins, mean temperatures, and evaporation barriers (or mean deformations) can be extracted from the fits to the data (see Figs. 9–14). It is important to stress here that the combined power of the observed energy and angular distributions impose rather stringent constraints for establishing these statistical-model parameters for the composite nuclear emitters.

The effect of each parameter on the calculated spectra has been discussed in detail elsewhere.[37] In brief, for spherical emitters there are three important variables: the s-wave emission barrier B_s, the temperature T, and the spin J. A change in the barrier dictates an overall shift in the calculated energy spectrum of the emitted particle. A change in the temperature (or excitation energy) dictates a change in the slope of the spectrum at high energies. A change in the spin dictates an alteration in the angular distribution of the particles with respect to the spin of the emitter (i.e., the out-of-plane angular distribution). This anisotropy is essentially controlled by $J_{\rm rms}^2/\mathcal{J}T$, and thus it can be related to the moment of inertia $\mathcal{J}$ if one has independent information on $J_{\rm rms}$ and T. In these studies the values of J are constrained by the spin zones given in Table II and the temperatures are constrained by the spectral shapes. For deformed emitters there are also three parameters, the mean deformation, the temperature, and the spin. Here a change in the deformation generates changes in both the emission barriers and the moments of inertia, as well as the rotational energy.

For emission from the fragments (both FF and QF), spherical nuclei were assumed and the barriers (^{1}H and ^{4}He) for these emitters were taken from systematics of evaporation barriers[65] summed over the Z distribution of the QF or FF fragments. No parameters were varied in these fits for the FE contributions. In fact, the details of the intrinsic evaporation parameters have been shown to have minimal effect on the calculated FE spectra because of the smearing due to the velocity distribution of the fragments.

By contrast, for CE it was necessary to vary these intrinsic evaporation parameters in order to obtain good fits to the data. Spin zones were taken from the cross section data for ER, FF, and QF as given in Table II. An initial set of evaporation barriers was obtained by fits to the in-plane data (for FF and QF) with the assumption of spherical emitters. The (spherical) barriers required ($B_s \approx 9.0$ MeV and 5.5 MeV for ^{4}He and ^{1}H, respectively) are substantially smaller than the corresponding fusion barriers ($B_{\rm fusion} \approx 16.0$ MeV and 8.5 MeV).[82] Such very low effective barriers suggest extensive deformation of the composite nuclei, and this possibility is discussed further in the next section. The effective temperatures of the composite-nucleus emitters require an average loss of excitation energy of $\approx 15\%$ prior to charged-particle emission. This fractional energy loss (FEL) is equivalent to the emission of ≈ 3 neutrons and is dictated primarily by the slopes of the various energy spectra. It implies that the particles are emitted over a range of steps in the evaporation chain. We simulate this range by an average or mean step, characterized by a set of mean parameters.

C. Distortions of the composite nuclei

A recurring theme for many recent particle-emission studies has been the very low barriers (^{1}H and ^{4}He) required for the characterization of evaporation spectra. These and other observations have been identified as evidence for shape and/or size evolution of hot rotating nuclei.[2,9,29,35,36,43,83,84] We explore the possible role of deformation in these data for ^{40}Ar + $^{\rm nat}$Ag via a series of calculations that assume a deformed composite nucleus. The calculations, performed with GANES,[37] simulate particle evaporation from deformed emitters whose barriers are determined by the extent of their deformation. It is important to reemphasize that, in these calculations, the evaporation barriers are not free parameters (as they are for assumed spherical emitters). The spectrum of barriers, for a given deformation, is calculated relative to the corresponding empirical fusion barrier[82] taken from reactions between cold, near-spherical nuclei.

Calculations were made with two free parameters: (a) the deformation and (b) the fractional energy loss; the spin was fixed by reference to the cross sections for ER, FF, and QF. In Table IV we summarize the set of statistical-model parameters that give the best fits to the observed CE energy and angular distributions. This set applies to both ^{1}H and ^{4}He emission for coincidences with both FF and QF (Figs. 9–14). These calculations required a rather extended prolate emitter with an axis ratio of ≈ 2.8. Such a strongly deformed emitter provides a good characterization of the low effective barrier for ^{4}He and the large moment of inertia $\mathcal{J}$ needed to fit the energy spectra and out-of-plane distributions. The need for a large moment of inertia is especially indicated by the out-of-plane angular correlations.

Figure 15 shows the relative probability $[W(\varphi_{l_0})]$ for alpha detection as a function of the angle with respect to the spin (φ_{l_0}) of the composite system. The dashed curves represent the calculated angular correlations for emission from a deformed emitter. These angular correlations were calculated with the parameters given in

TABLE IV. Statistical properties of the composite-nucleus emitters in FF and QF (Figs. 9–14).

$J_{rms}(\hbar)$ FF	87 (337 MeV)	82 (247 MeV)[a]
$J_{rms}(\hbar)$ QF	123 (337 MeV)	103 (247 MeV)[a]
$\bar{\epsilon}$	0.8[b]	
b/a	2.8[b]	
$\mathcal{J}_\perp/\mathcal{J}_0$	2.35[c]	
$\mathcal{J}_\parallel/\mathcal{J}_0$	0.54[c]	
B_{max} (MeV)	16.7(α)8.7(p)[d]	
B_{min} (MeV)	12.9(α)6.7(p)[d]	
B_{fusion}	16.0(α)8.5(p)[e]	
⟨FEL⟩	0.15[f]	
T (MeV) FF	2.9 (337 MeV)	2.2 (247 MeV)[g]
T (MeV) QF	2.6 (337 MeV)	2.0 (247 MeV)[g]

[a]Root-mean-square spin of the emitter. Chosen to be consistent with the spin zones given in Table II.

[b]Cassini deformation parameter (Ref. 37) $\bar{\epsilon}$ and associated axis ratio (b/a) of the deformed daughter nucleus.

[c]Moment of inertia perpendicular (parallel) to the symmetry axis compared to that of the sphere. These values are derived from the value selected for $\bar{\epsilon}$.

[d]Barrier height for particle emission at the waist (max) or at the tips (min) of the prolate spheroid (values dependent on $\bar{\epsilon}$). The average effective evaporation barrier is about B_{min} plus $\approx\frac{1}{2}(B_{max}-B_{min})$, substantially smaller than B_{fusion}.

[e]Empirical barriers for fusion between cold nuclei (Ref. 82).

[f]Fractional excitation energy lost (FEL) to particle emission (or deformation) prior to the average particle emission.

[g]Mean temperature of the daughter. These values result from the value selected for ⟨FEL⟩ above.

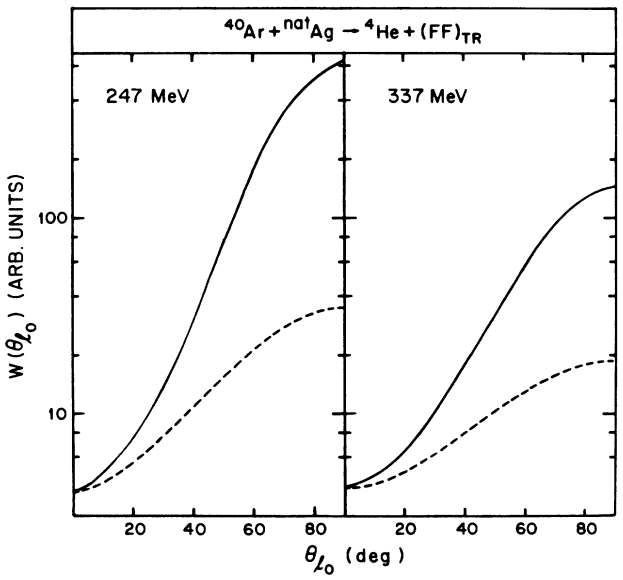

FIG. 15. Simulated out-of-plane angular correlations (c.m.) for CE α-particle emission in coincidence with FF triggers ($\varphi_{l_0}=90°$ and 0° represent particle detection perpendicular and parallel to the spin of the composite system, respectively). The dashed curves represent the angular correlations from simulations for a deformed nucleus. Both these curves correspond to the good fits of Figs. 9 and 10. The solid curves are the calculated out-of-plane correlations for emission from a spherical nucleus. These latter calculations do not fit the data in Figs. 9(b) and 10(b).

Table IV as obtained from the fits for ^{4}He in Figs. 9 and 10. Consequently, they effectively represent the out-of-plane correlations from the data. Calculated out-of-plane correlations, for emission from a spherical nucleus of the same spin, are shown as solid curves in Fig. 15. The anisotropies calculated for deformed emitters are $\approx 10-20$ times smaller than those for spherical emitters. This large difference between spherical and deformed emitters is due to the different moments of inertia. The experimental data for ^{4}He emission are well simulated by a strongly deformed emitter and are totally incompatible with simulations for a spherical emitter. Similar results have been reported in Ref. 29. The results for ^{1}H are much less extensive than those for ^{4}He, and although they are consistent with the same emitter parameters, they do not supply very strong constraints. A systematic discussion of the role of spin and deformation in these simulations is given in Ref. 37.

The very large effective deformation inferred for the composite system ($b/a\approx 2.8$) is larger than that for an equilibrium shape as predicted by the rotating liquid drop model.[68] Hence, it is proposed that these results suggest a dinuclear complex enroute to fission; such a complex has been discussed in the calculations of Gregoire *et al.*[85] and Feldmeier.[86] In the next section some additional results are presented that are also consistent with this notion.

D. Near scission emission and proximity effects

In the last few years, two new and intriguing aspects of particle-emission processes have been reported,[29,31,66,67,71] near scission emission (NSE) and shadowing. The shadowing phenomenon has been used to extract information on the lifetime of fission fragments, and the CE multiplicities have been used to infer similar information for composite nuclei.[5,29,87] Similarly, NSE has provided new insight concerning the evolution of composite systems on their dynamic paths to scission. Signatures for both NSE and shadowing processes have been noted in this work also (Sec. IV). Further discussion of their mechanistic implications is pursued in this section.

The particles assigned to the NSE process in Sec. IV [i.e., the excess of intermediate energy particles at position 1 in Figs. 9(b) and 10(b)] exhibit a number of characteristics which serve as clues to their origin. First, it is important to point out that NSE shows a dependence on bombarding energy which is very similar to that exhibited by FE and CE. Second, the energy distributions of these NSE particles (intermediate between FE and CE) are consistent with very low effective barriers. These results corroborate previous findings[66,71] and give evidence for the evaporative nature of these particles. Third, the NSE particles in this work are not prominently observed in-plane, but they do appear with clarity out-of-plane. This observation of prominent out-of-plane emission is consistent with the well established pattern for NSE (enhanced emission at angles perpendicular to the scission axis).[31,67] Brucker *et al.*[66] indicate the presence of NSE with special clarity in the reaction plane. In this

work detector thresholds prevent us from getting a clear view at the in-plane angles expected to be most crucial. We can only say that particles of intermediate energy are observed for out-of-plane configurations that could be accounted for by NSE. From information of this type, several groups have suggested that these particles may be emitted from the "neck" of an elongated dinuclear system. A detailed study of the angular distributions of these particles (in and out-of-plane[71]) has provided interesting insight into their emission time relative to the rotation time of the elongated emitter nucleus.

The NSE observed in the out-of-plane configuration for the FF mechanism is not evident in the QF results [see Fig. 12(b)]. By contrast a suggestion of shadowing was shown for QF processes in Fig. 13. The absence of NSE signatures in the QF results could suggest rapid decay of the dinuclear complexes formed in these reactions. However, the shadowing phenomenon suggests that particle emission times for newly born fragments are comparable to fragment acceleration times. It may be that the relative prominence for NSE versus that for shadowing is giving us hints on the relative time duration of evaporation from the neck versus fragment acceleration. Our (admittedly limited) results on this point indicate NSE for FF and shadowing but very much less NSE for QF. This

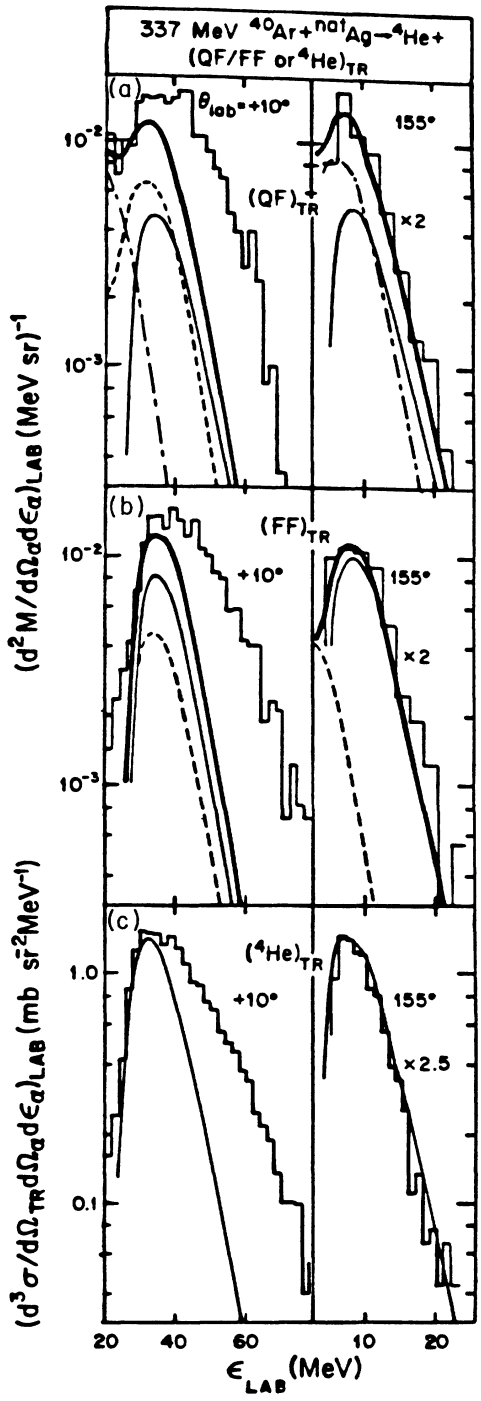

FIG. 16. Coincidence spectra for ^{4}He at 10° and 155° to the beam for various triggers: (a) QF, (b) FF, and (c) ^{4}He. The ^{4}He trigger can be largely identified with the ER's and hence these figures typify the spin zones given in Table II. Same notation as in Figs. 9–15.

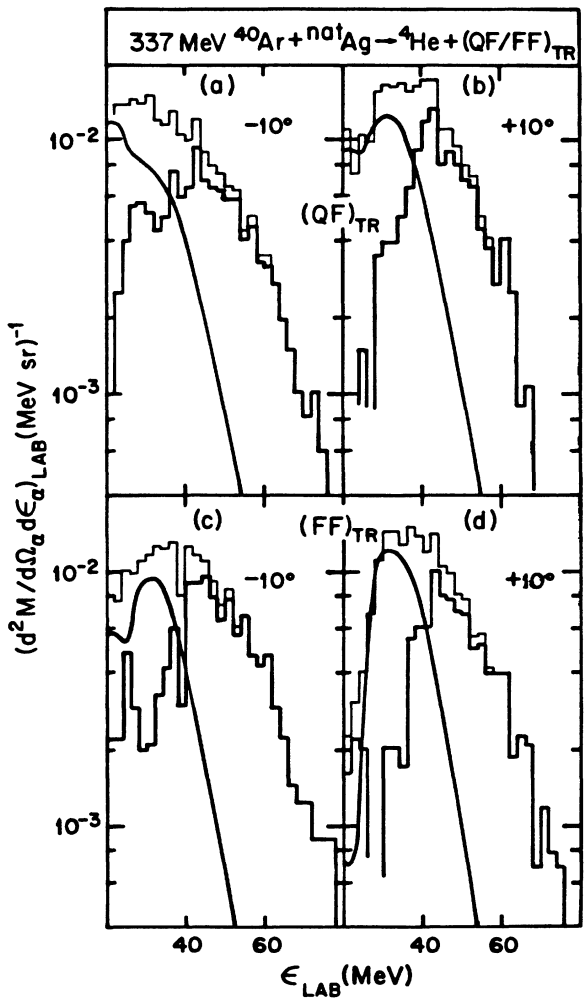

FIG. 17. Comparison of spectra at 10° and −10° for QF and FF triggers. Thin-lined histograms represent the data, smooth curves represent the evaporation simulation for CE plus FE, and thick-lined histograms give their difference, i.e., the PTE and NSE components.

situation implies that a longer period for neck rupture in FF gives rise to NSE, and that a shorter time for neck rupture in QF suppresses NSE. The shadowing for QF implies a rapid initiation of evaporation from fragments before they move far apart.

VI. PRETHERMALIZATION EMISSION (PTE)

Figure 2 above shows a clear forward peak in the angular distribution of the emitted particles. From the inclusive data alone, one cannot distinguish the extent of evaporative emission from the forward-peaked, projectilelike fragments. Therefore, he cannot be sure whether or not prethermalization emission has actually occurred. In Figs. 9–14 we show reaction simulations that account for the bulk of the overall ^{1}H and ^{4}He emission in terms of statistical evaporation. However, in Figs. 9(a) and 12(a) we see (at $+10°$ and $-10°$) a distinct excess of ^{4}He emission especially at high energies. In these figures we have accounted for evaporation from each fragment and thus this excess must be from PTE.

Figure 16 emphasizes this point by comparing the data at 10° and 155° for three coincidence triggers (a) QF, (b) FE, and (c) ^{4}He. The simulation calculations are normalized so as to describe the results at backward angles, but they underpredict the results at 10°. The relative amounts of PTE and evaporative emission are comparable for the three coincidence triggers. As mentioned above, the ^{4}He trigger emphasizes emission from the evaporation residues and hence the most central collisions. Thus from the discussion of Table II we can associate PTE in comparable amounts with each spin zone $0-70\hbar$ for the ^{4}He trigger, $70-103\hbar$ for FF and $103-133\hbar$ for QF.

The presence or absence of right-left symmetry can also give some insight into the combination of particle and fragment emission times. In Fig. 17 we show a comparison of ^{4}He spectra observed at $+10°$ and $-10°$ to the beam. Light histograms give the raw data, smooth curves the evaporation simulations, and dark histograms show the differences. For both FF and QF triggers, the high-energy α spectra ($\epsilon_\alpha > 40$ MeV) are very similar on the right and left sides. (This result differs from that reported in Ref. 71.) However, for the lowest energies ($\epsilon_\alpha < 30$ MeV) there seems to be a preference for $-10°$. This asymmetry for $\epsilon_\alpha < \approx 30$ MeV could be explained by near scission emission as discussed above in Sec. IV D. An absence of distinct right-left asymmetry for $\epsilon_\alpha > 40$ MeV implies a substantial rotation of the scission axis between the instant of particle ejection and that of scission. This result would indicate a strong contrast between the times for PTE and NSE as compared to the rotation time.

VII. SUMMARY

In Secs. IV–VI, various features of the fragment-particle correlation measurements for 247 and 337 MeV ^{40}Ar + ^{nat}Ag have been presented and discussed. The major findings are as follows.

(a) Substantial particle emission (^{1}H and ^{4}He) occurs in both FF and QF reactions, but the largest fraction of the particle production cross section ($\approx 75\%$ and 50% for the 247 and 337 MeV beams, respectively) is associated with the evaporation residues.

(b) Due to relatively low detection thresholds and a wide angle span for the experimental geometry, it was possible to identify clear signatures for several emission processes and to determine multiplicities for CE and FE.

(c) Energy and angular distributions of ^{1}H and ^{4}He were found to be consistent with the major features of statistical evaporation. In particular FE and CE provide an adequate description for most of the experimental data.

(d) A decrease in CE multiplicity for both ^{1}H and ^{4}He was observed for QF as compared to FF. This decrease of $\approx 1/2$ (1/4) for 337 MeV ^{40}Ar (247 MeV ^{40}Ar) implies a similar ratio for the relative lifetimes of the composite systems.

(e) A deformed composite nucleus with axis ratio $b/a \approx 2.8$ was found to be compatible with the low effective particle evaporation barriers and the comparatively weak out-of-plane angular anisotropies observed for ^{4}He from composite nucleus emission prior to FF and QF.

(f) An observed excess of intermediate energy particles out-of-plane is consistent with near scission emission with enhanced emission perpendicular to the scission axis.

(g) At angles close to the detected QF fragments a deficit of particles emitted by the undetected fragments was observed. This finding is consistent with previous observations of the "shadowing" phenomenon.[29,69]

(h) Prethermalization emission was found to be present in comparable amounts for the peripheral collisions triggered by QF and FF reactions as well as the central collisions associated with the ER's.

ACKNOWLEDGMENTS

This work is based in part on the Ph.D. thesis of one of the authors (R.L.) Department of Chemistry, State University of New York at Stony Brook, Stony Brook, N.Y. 11794. We wish to thank the staff of the LBL SuperHILAC for its very fine support. Particularly we thank W. Rathbun for his help with the data-acquisition system. This work was mainly supported by the Division of Nuclear Physics, Office of High Energy and Nuclear Physics, U.S. Department of Energy.

---

*Permanent address: Bhabha Atomic Research Centre, Nuclear Physics Division, Trombay 400085, Bombay, India.

†Permanent address: Department of Chemistry, Middle East Technical University, Ankara, Turkey.

‡Permanent address: Instituto di Fisica Sperimentale, Mostra d'Oltremare, Napoli 80125, Italy.

§Permanent address: International Business Machines, Kingston, NY 12401.

**Permanent address: Department of Physics, Hope College, Holland, MI 49423.

[1]R. Bass, *Nuclear Reactions with Heavy Ions* (Springer-Verlag, New York, 1980).

[2]L. C. Vaz, D. Logan, E. Duek, J. M. Alexander, M. F. Rivet, M. S. Zisman, M. Kaplan, and J. W. Ball, Z. Phys. A **315**, 169 (1984).

[3]N. N. Ajitanand, J. M. Alexander, H. Delagrange, E. Duek, D. O. Eriksen, D. Guerreau, M. Kaplan, M. Kildir, L. Kowalski, R. Lacey, D. Logan, D. J. Moses, G. F. Peaslee, L. C. Vaz, and M. S. Zisman, Z. Phys. A **316**, 169 (1984).

[4]D. Hilscher, H. Rossner, A. Gamp, U. Jahnke, B. Chenis, B. Chambon, D. Drain, C. Pastor, A. Giorni, C. Morand, A. Dauchy, P. Stassi, and G. Petitt, Phys. Rev. C **36**, 208 (1987).

[5]A. Gavron, A. Gayer, J. Boissevain, H. C. Britt, T. C. Awes, J. R. Beene, B. Cheynis, D. Drain, R. L. Ferguson, F. E. Obenshain, F. Plasil, G. R. Young, G. A. Petitt, and C. Butler, Phys. Rev. C **35**, 579 (1987).

[6]M. Fatyga, H. J. Karwowski, K. Kwiatkowski, L. Nowicki, V. E. Viola, and H. Hicks, Phys. Rev. C **35**, 568 (1987); M. Fatyga, R. C. Bryd, K. Kwiatkowski, W. G. Wilson, L. W. Woo, V. E. Viola, Jr., H. J. Karwowski, J. Jastrzebski, and W. Skulski, Phys. Lett. **185B**, 321 (1987).

[7]B. A. Remington, G. Caskey, A. Galonsky, C. K. Gelbke, L. Heilbronn, J. Heltsley, M. B. Tsang, F. Deak, A. Kiss, Z. Seres, J. Kasagi, and J. J. Kolata, Phys. Rev. C **34**, 1686 (1986).

[8]Y. Patin, S. Leray, E. Tomasi, O. Granier, C. Cerruti, J. L. Charvet, S. Chiodelli, A. Demeyer, D. Guinet, C. Humeau, P. Lhenoret, J. P. Lochard, R. Locus, C. Mazur, M. Morjean, C. Ngo, A. Peghaire, M. Ribrag, L. Sinopoli, T. Suomijarvi, J. Uzureau, and L. Vagneron, Nucl. Phys. **A547**, 146 (1986).

[9]Z. Majka, M. E. Brandan, D. Fabris, K. Hagel, A. Menchaca-Rocha, J. B. Natowitz, G. Nebbia, G. Prete, B. Sterling, and G. Viesti, Phys. Rev. C **35**, 2125 (1987).

[10]D. J. Hinde, R. J. Charity, G. S. Foote, J. R. Leigh, J. O. Newton, S. Ogaza, and A. Chattejee, Nucl. Phys. **A452**, 550 (1986).

[11]R. J. Charity, M. A. McMahan, D. R. Bowman, Z. H. Liu, R. J. McDonald, G. J. Wozniak, L. G. Moretto, S. Bradley, W. L. Kehoe, A. C. Mignerey, and M. N. Namboodiri, Phys. Rev. Lett. **56**, 1354 (1986).

[12]G. S. F. Stephans, D. G. Kovar, R. V. F. Janssens, G. Rosner, H. Ikezoe, B. Wilkins, D. Henderson, K. T. Lesko, J. J. Kolata, C. K. Gelbke, B. V. Jacak, Z. M. Koenig, G. D. Westfall, A. Szanto de Toledo, E. M. Szanto, and P. L. Gonthier, Phys. Lett. **161B**, 60 (1985).

[13]M. J. Murphy, D. Leach, A. Ray, A. Seamster, and R. Vandenbosch, Phys. Rev. C **33**, 165 (1986).

[14]J. L. Laville, C. Le Brun, J. F. Lecolley, F. Lefebvres, M. Louvel, R. Regimbart, J. C. Steckmeyer, R. Bertholet, C. Guet, D. Heuer, M. Maurel, H. Nifenenecker, C. Ristori, F. Schlussler, F. Guilbault, and C. Lebrun, Phys. Lett. **156B**, 42 (1985).

[15]D. Jacquet, J. Galin, B. Borderie, D. Gardes, D. Guerreau, M. Lefort, F. Monnet, M. F. Rivet, X. Tarrago, E. Duek, and J. M. Alexander, Phys. Rev. C **32**, 1594 (1985).

[16]C. Gerschel, A. Gillibert, N. Perrin, and H. Tricoire, Z. Phys. A **322**, 433 (1985).

[17]S. B. Gazes, R. P. Boisseau, L. Grodzins, A. P. Smith, and S. G. Steadman, Phys. Lett. **153B**, 33 (1985).

[18]H. Fuchs, M. Burgel, H. Homeyer, G. Ingold, U. Jahnke, and G. Thoma, Phys. Rev. C **31**, 465 (1985).

[19]J. P. Kosky, W. W. Wilcke, J. R. Birkelund, M. A. Butler, A. D. Dougan, J. R. Huizenga, W. U. Schroder, H. J. Wollersheim, and D. Hilscher, Phys. Lett. **133B**, 153 (1983).

[20]S. Song, M. F. Rivet, R. Bimbot, B. Borderie, I. Forest, J. Galin, D. Gardes, B. Gatty, M. Lefort, H. Oeschler, B. Tamain, and X. Tarrago, Phys. Lett. **130B**, 14 (1983).

[21]D. J. Moses, M. Kaplan, M. Kildir, D. R. G. Logan, G. La Rana, W. E. Parker, R. Lacey, G. F. Peaslee, J. M. Alexander, N. N. Ajitanand, L. C. Vaz, and M. S. Zisman, Nucl. Phys. **A465**, 339 (1987).

[22]A. Ruckelshausen, R. D. Fischer, W. Kuhn, V. Metag, R. Muhlhans, R. Novotny, T. L. Khoo, R. V. F. Janssens, H. Groger, D. Habs, H. W. Heyng, R. Repnow, D. Schwalm, G. Duchene, R. M. Freeman, B. Haas, F. Haas, S. Hlavac, and R. S. Simon, Phys. Rev. Lett. **56**, 2356 (1986).

[23]U. Jahnke, G. Ingold, D. Hilscher, M. Lehmann, E. Schwinn, and P. Zank, Phys. Rev. Lett. **57**, 190 (1986).

[24]E. Holub, D. Hilscher, G. Ingold, U. Jahnke, H. Orf, H. Rossner, W. P. Zank, W. U. Schroder, H. Gekmmeke, K. Keller, L. Lassen, and W. Lucking, Phys. Rev. C **33**, 143 (1986).

[25]A. Gavron, A. Gayer, J. Boissevain, H. C. Britt, J. R. Nix, A. J. Sierk, P. Grange, S. Hassani, H. A. Weidenmuller, J. R. Beene, B. Cheynis, D. Drain, R. L. Ferguson, F. E. Obenshain, F. Plasil, G. R. Young, G. A. Petitt, and C. Butler, Phys. Rev. Lett. **176B**, 312 (1986).

[26]G. A. Petitt, A. Gavron, J. R. Beene, B. Cheynis, R. L. Gerguson, F. E. Obenshain, F. Plasil, G. R. Young, M. Jaaskelainen, D. G. Sarantites, and C. F. Maguire, Phys. Rev. C **32**, 1572 (1985).

[27]D. J. Moses, M. Kaplan, J. M. Alexander, D. Logan, M. Kildir, L. C. Vaz, N. N. Ajitanand, E. Duek, and M. S. Zisman, Z. Phys. A **320**, 229 (1985).

[28]H. Ho, G.-Y. Fan, P. L. Gonthier, W. Kuhn, B. Lindl, A. Pfoh, L. Schad, R. Wolski, J. P. Wurm, J. C. Adloff, D. Disdier, V. Rauch, and F. Scheibling, Nucl. Phys. **A437**, 465 (1985).

[29]L. Schad, H. Ho, G.-Y. Fan, B. Lindl, A. Pfoh, R. Wolski, and J. P. Wurm, Z. Phys. A **318**, 179 (1984).

[30]M. Kildir, D. Logan, D. O. Eriksen, D. J. Moses, M. Kaplan, E. Duek, L. C. Vaz, N. N. Ajitanand, J. M. Alexander, and M. S. Zisman, Z. Phys. A **317**, 291 (1984).

[31]E. Duek, N. N. Ajitanand, J. M. Alexander, D. Logan, M. Kildir, L. Kowalski, L. C. Vaz, D. Guerreau, M. S. Zisman, M. Kaplan, and D. J. Moses, Z. Phys. A **317**, 83 (1984).

[32]C. Borcea, E. Gierlik, R. Kalpakchieva, N. H. Chau, Y. T. Oganessian, T. Pawlat, Y. E. Penionzhkevich, Nucl. Phys. **A415**, 169 (1984).

[33]T. Ericson, Adv. Phys. **9**, 423 (1960).

[34]T. Dossing, Licentiat thesis and unpublished notes. University of Copenhagen, Denmark (1977); S. M. Vydrug-Vlasenko, V. F. Zavarzin, and S. Yu Kun, Yad. Fiz. **41**, 117 (1985).

[35]G. La Rana, D. J. Moses, W. E. Parker, M. Kaplan, D. Logan, R. Lacey, J. M. Alexander, and R. J. Welberry, Phys. Rev. C **35**, 373 (1987).

[36]R. Lacey, N. N. Ajitanand, J. M. Alexander, D. M. de Castro Rizzo, P. DeYoung, M. Kaplan, L. Kowalski, G. La Rana, D. Logan, D. J. Moses, W. E. Parker, G. F. Peaslee, and L. C. Vaz, Phys. Lett. B **191**, 253 (1987).

[37]N. N. Ajitanand, R. Lacey, G. F. Peaslee, E. Duek, and J. M. Alexander, Nucl. Instrum. Methods Phys. Res. A **243**, 111 (1986). N. N. Ajitanand, G. La Rana, R. Lacey, D. J. Moses, L. C. Vaz, G. F. Peaslee, D. M. de Castro Rizzo, M. Kaplan, and J. M. Alexander, Phys. Rev. C **34**, 877 (1986).

[38]H. C. Britt, B. H. Erkkila, R. H. Stokes, H. H. Gutbrod, F. Plasil, R. L. Ferguson, and M. Blann, Phys. Rev. C **13**, 1483

(1976).

[39]R. Lacey, N. N. Ajitanand, J. M. Alexander, D. M. de Castro Rizzo, G. F. Peaslee, L. C. Vaz, M. Kaplan, M. Kildir, G. La Rana, D. J. Moses, W. E. Parker, D. Logan, M. S. Zisman, P. DeYoung, and L. Kowalski, following papers Phys. Rev. C **37**, 2560 (1988).

[40]D. J. Moses, Ph.D. dissertation, Dept. of Chemistry, Carnegie-Mellon University (1986).

[41]M. M. Fowler and R. C. Jared, Nucl. Instrum. Methods **124**, 341 (1975).

[42]S. B. Kaufman, E. P. Steinberg, B. D. Wilkins, J. Unik, A. J. Gorski, and M. J. Fluss, Nucl. Instrum. Methods **115**, 47 (1974).

[43]R. Lacey, N. N. Ajitanand, J. M. Alexander, D. M. de Castro Rizzo, G. F. Peaslee, L. C. Vaz, G. La Rana, M. Kaplan, D. J. Moses, W. Parker, D. Logan, and P. DeYoung, J. Phys. (Paris) Colloq. **C-4**, 289 (1986).

[44]A. G. Artukh, V. V. Avdelchikov, G. F. Gridnev, M. Gruzecki, W. Karcz, A. N. Mezentsev, V. L. Mikheev, V. M. Morozov, L. Pomorski, A. Popescu, D. G. Popescu, and V. V. Volkov, Soc. J. Nucl. Phys. **38**, 326 (1983).

[45]H. C. Britt and A. R. Quinton, Phys. Rev. **124**, 877 (1961).

[46]D. Logan, M. Rajagopalan, M. S. Zisman, J. M. Alexander, M. Kaplan, and L. Kowalski, Phys. Rev. C **22**, 104 (1980).

[47]D. Logan, H. Delagrange, M. F. Rivet, M. Rajagopalan, J. M. Alexander, M. Kaplan, M. S. Zisman, and E. Duek, Phys. Rev. C **22**, 1080 (1980).

[48]T. C. Awes, S. Saini, G. Poggi, C. K. Gelbke, D. Cha, R. Legrain, and G. D. Westfall, Phys. Rev. C **25**, 2361 (1982).

[49]M. Rajagopalan, D. Logan, J. W. Ball, M. Kaplan, H. Delagrange, M. F. Rivet, J. M. Alexander, L. C. Vaz, and M. S. Zisman, Phys. Rev. C **25**, 2417 (1982).

[50]M. F. Rivet, D. Logan, J. M. Alexander, D. Guerreau, E. Duek, M. S. Zisman, and M. Kaplan, Phys. Rev. C **25**, 2430 (1982).

[51]D. Guerreau, D. Logan, M. F. Rivet, E. Duek, L. C. Vaz, J. M. Alexander, L. Kowalski, and M. S. Zisman (unpublished).

[52]J. Galin, B. Gatty, D. Guerreau, C. Rousset, U. C. Schlotthauer-Voos, and X. Tarrago, Phys. Rev. C **9**, 1113 (1974); J. Galin, B. Gatty, D. Guerreau, C. Rousset, U. C. Schlotthauer-Voos, and X. Tarrago, *ibid.* **9**, 1126 (1974).

[53]R. C. Reedy, J. J. Fluss, G. F. Herzog, L. Kowalski, and J. M. Miller, Phys. Rev. **188**, 1771 (1969).

[53]J. Galin, L. G. Moretto, R. Babinet, R. Schmitt, D. R. Jared, and S. G. Thompson, Nucl. Phys. **A255**, 472 (1975).

[55]H. H. Gutbrod, F. Plasil, H. C. Britt, B. H. Erkkila, R. H. Stokes, M. Blann, *Proceedings of the 3rd IAEA Symposium on the Physics and Chemistry of Fission, Rochester, 1973* (IAEA, Vienna, 1974), Vol. II, p. 309.

[56]W. Trautman, J. de Boer, W. Dunnweber, G. Grau, R. Kopp, C. Lauterbach, and H. Puchta, U. Lynen, Phys. Rev. Lett. **39**, 1062 (1977).

[57]A. G. Arthukh, G. F. Gridnev, M. Gruszecki, W. Karcz, A. N. Mezentsev, V. L. Mikheev, L. Pomorski, A. Popescu, D. G. Popescu, and V. V. Volkov, Z. Phys. A **303**, 41 (1981).

[58]L. C. Vaz, D. Logan, J. M. Alexander, E. Duek, D. Guerreau, L. Kowalski, M. F. Rivet, and M. S. Zisman, Z. Phys. A **311**, 89 (1983).

[59]T. W. Armstrong and K. C. Chandler, Oak Ridge National Laboratory Internal Report (Mathematics Division) ORNL-4869, May 1973.

[60]D. L. Hill, J. A. Wheeler, Phys. Rev. **89**, 1102 (1953).

[61]A. Bohr, in *Proceedings of the International Conference on the Peaceful Uses of Atomic Energy, Geneva, 1955* (United Nations, New York, 1956), Vol. 2, p. 131.

[62]I. Halpern and V. M. Strutinsky, in *Proceedings of the International Conference on the Peaceful Uses of Atomic Energy, Geneva, 1955* (United Nations, New York, 1956), p. 398.

[63]J. A. Wheeler, in *Fast Neutron Physics*, edited by J. B. Marion and J. L. Fowler (Wiley, New York, 1963), Pt. 2.

[64]R. Freifelder, M. Prakash, and J. M. Alexander, Phys. Rep. **133**, 315 (1986).

[65]W. E. Parker, R. J. Welberry, D. J. Moses, and M. Kaplan, Carnegie-Mellon University Annual Report No. COO-3246-25, 1985 (unpublished).

[66]A. Brucker, B. Lindl, M. Bantel, H. Ho, R. Muffler, L. Schad, M. G. Trauth, and J. P. Wurm, Phys. Lett. **B186**, 20 (1987).

[67]E. Duek, N. N. Ajitanand, J. M. Alexander, D. Logan, M. Kildir, L. Kowalski, L. C. Vaz, D. Guerreau, M. S. Zisman, and M. Kaplan, Phys. Lett. **131B**, 297 (1983).

[68]S. Cohen, F. Plasil, W. J. Swiatecki, Ann. Phys. (NY) **82**, 557 (1974).

[69]H. Ho, P. L. Gonthier, G. Y. Fan, W. Kuhn, A. Pfoh, L. Schad, R. Wolski, J. P. Wurm, J. C. Adloff, D. Disdier, A. Kamili, V. Rauch, G. Rudolf, F. Scheibling, and A. Strazzeri, Phys. Rev. C **27**, 584 (1983).

[70]G.-Y. Fan, H. Ho, P. L. Gonthier, W. Kuhn, A. Pfoh, L. Schad, R. Wolski, J. P. Wurm, J. C. Adloff, D. Disdier, V. Rauch, and F. Scheibling, Z. Phys. A **310**, 269 (1983).

[71]B. Lindl, A. Brucker, M. Bantel, H. Ho, R. Muffler, L. Schad, M. G. Trauth and J. P. Wurm, Z. Phys. **A328**, 85 (1987).

[72]M. G. Mustafa, P. A. Baisden, and H. Chandra, Phys. Rev. C **25**, 2524 (1982).

[73]A. J. Sierk, Phys. Rev. C **33**, 2029 (1986).

[74]N. Bohr and J. A. Wheeler, Phys. Rev. **56**, 426 (1939).

[75]W. Hauser and H. Feshbach, Phys. Rev. **87**, 336 (1952); A. C. Douglas and N. MacDonald, Nucl. Phys. **13**, 382 (1959).

[76]J. M. Alexander, H. Delagrange, M. Rajagopalan, M. F. Rivet, and L. C. Vaz, Z. Phys. A **307**, 149 (1982).

[77]P. Grange, J. Q. Li, and H. A. Weidenmuller, Phys. Rev. C **27**, 2063 (1983).

[78]H. A. Kramers, Physica **40**, 284 (1940).

[79]W. Westheimer and R. A. Esterlund, Z. Phys. A **316**, 27 (1984).

[80]P. J. Grange, S. Hassini, H. A. Weidenmuller, A. Gavron, J. R. Nix, and A. J. Sierk, Phys. Rev. C **34**, 2063 (1986).

[81]E. Hofmann and J. R. Nix, Phys. Lett. **122B**, 117 (1983).

[82]L. C. Vaz and J. M. Alexander, Z. Phys. A **318**, 231 (1984).

[83]D. J. Moses, M. Kaplan, G. La Rana, W. E. Parker, R. Lacey, and J. M. Alexander, Phys. Rev. C **36**, 422 (1987).

[84]F. A. Dilmanian, D. G. Sarantites, M. Jaaskelainen, H. Puchta, R. Woodward, J. R. Beene, D. C. Hensley, M. L. Halbert, R. Novotny, L. Adler, R. K. Choudhury, M. N. Namboodiri, R. P. Schmitt, and J. B. Natowitz, Phys. Rev. Lett. **49**, 1909 (1982).

[85]C. Gregoire, C. Ngo, and B. Remaud, Phys. Lett. **99B**, 17 (1981).

[86]H. Feldmeier, *Nuclear Structure on Heavy Ion Dynamics*, Proceedings of the International School of Physics "Enrico Fermi," Varenna, 1982, (North-Holland, Amsterdam, 1982), p. 274.

[87]W. P. Zank, D. Hilscher, G. Ingold, U. Jahnke, M. Lehmann, and H. Rossner, Phys. Rev. C **33**, 519 (1986).

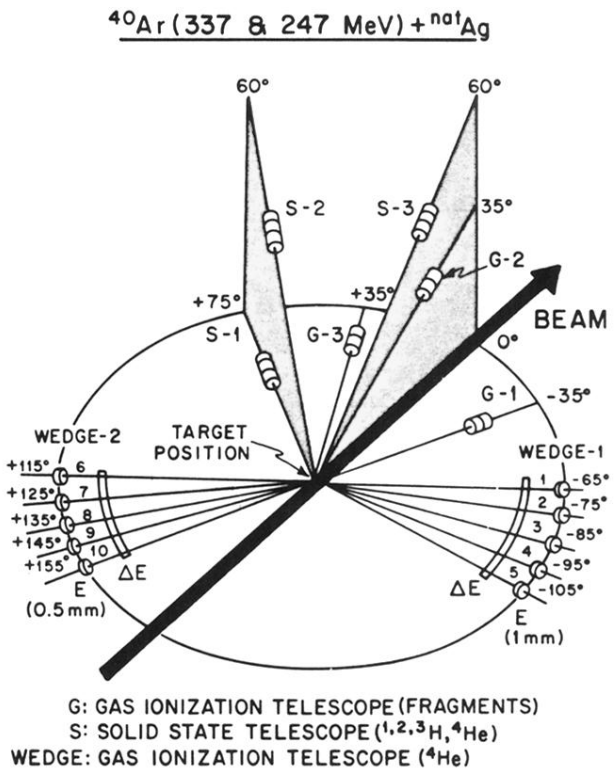

FIG. 1. Detector setup for this study of the reactions 247 and 337 MeV $^{40}Ar + {}^{nat}Ag$. Heavy fragments are detected in three gas ionization telescopes (G-1,-2,3). Light charged particles (H and He) were detected in three solid state telescopes (S-1,-2,-3) and two $\Delta E - E$ wedge detectors (W-1 and W-2).